

A new dynamic approach for statistical optimization of GNSS radio occultation bending angles for optimal climate monitoring utility

Y. Li,¹ G. Kirchengast,² B. Scherllin-Pirscher,² S. Wu,¹ M. Schwaerz,² J. Fritzer,² S. Zhang,¹ B. A. Carter,¹ and K. Zhang¹

Received 18 August 2013; revised 30 October 2013; accepted 7 November 2013; published 10 December 2013.

[1] Global Navigation Satellite System (GNSS)-based radio occultation (RO) is a satellite remote sensing technique providing accurate profiles of the Earth's atmosphere for weather and climate applications. Above about 30 km altitude, however, statistical optimization is a critical process for initializing the RO bending angles in order to optimize the climate monitoring utility of the retrieved atmospheric profiles. Here we introduce an advanced dynamic statistical optimization algorithm, which uses bending angles from multiple days of European Centre for Medium-range Weather Forecasts (ECMWF) short-range forecast and analysis fields, together with averaged-observed bending angles, to obtain background profiles and associated error covariance matrices with geographically varying background uncertainty estimates on a daily updated basis. The new algorithm is evaluated against the existing Wegener Center Occultation Processing System version 5.4 (OPSv5.4) algorithm, using several days of simulated MetOp and observed CHAMP and COSMIC data, for January and July conditions. We find the following for the new method's performance compared to OPSv5.4: 1.) it significantly reduces random errors (standard deviations), down to about half their size, and leaves less or about equal residual systematic errors (biases) in the optimized bending angles; 2.) the dynamic (daily) estimate of the background error correlation matrix alone already improves the optimized bending angles; 3.) the subsequently retrieved refractivity profiles and atmospheric (temperature) profiles benefit by improved error characteristics, especially above about 30 km. Based on these encouraging results, we work to employ similar dynamic error covariance estimation also for the observed bending angles and to apply the method to full months and subsequently to entire climate data records.

Citation: Li, Y., G. Kirchengast, B. Scherllin-Pirscher, S. Wu, M. Schwaerz, J. Fritzer, S. Zhang, B. A. Carter, and K. Zhang (2013), A new dynamic approach for statistical optimization of GNSS radio occultation bending angles for optimal climate monitoring utility, *J. Geophys. Res. Atmos.*, 118, 13,022–13,040, doi:10.1002/2013JD020763.

1. Introduction

[2] Global Navigation Satellite System (GNSS) radio occultation (RO) is a satellite remote sensing technique to observe the properties of the Earth's atmosphere [Kursinski *et al.*, 1997; Steiner *et al.*, 2001; Hajj *et al.*, 2002]. This technique uses specially designed GNSS receivers aboard Low Earth Orbit (LEO) satellites to receive GNSS signals. So far, only GNSS signals from the U.S. Global Positioning System (GPS) have been used. Signals from other satellite navigation systems like the European Galileo or the Russian Global

Navigation Satellite System (GLONASS) are proposed to be used in near future. Due to the inhomogeneity of atmospheric density, and hence of the refractive index, GPS signals are bent during their propagation through the atmosphere. The bending angles can be calculated and used to derive atmospheric profiles such as of refractivity and temperature.

[3] Since the 1990s, a number of LEO missions have been carried out to perform GPS RO measurements, such as GPS/MET [Kursinski *et al.*, 1996; Ware *et al.*, 1996; Hocke, 1997; Rocken *et al.*, 1997; Steiner *et al.*, 1999], CHALLENGING Minisatellite Payload (CHAMP) [Wickert *et al.*, 2001, 2004], Constellation Observing System for Meteorology, Ionosphere, and Climate (COSMIC) [Anthes *et al.*, 2008], and the Meteorological Operational (MetOp) satellite program [Luntama *et al.*, 2008; von Engel *et al.*, 2009]. Apart from these existing missions, many other missions, e.g., COSMIC-2, are proposed to be launched during the coming years. All these missions can and will provide high-quality atmospheric profiles contributing to continuous long-term RO records.

[4] The RO technique exhibits several beneficial characteristics: First, its measurements are self-calibrating and long-term stable, which makes data from multiple RO satellites highly

¹Satellite Positioning for Atmosphere, Climate, and Environment (SPACE) Research Centre, RMIT University, Melbourne, Victoria, Australia.

²Wegener Center for Climate and Global Change (WEGC) and Institute for Geophysics, Astrophysics, and Meteorology/Institute of Physics (IGAM/IP), University of Graz, Graz, Austria.

Corresponding author: Y. Li, Satellite Positioning for Atmosphere, Climate, and Environment (SPACE) Research Centre, RMIT University, Melbourne, Australia. (lovewudl23.ying.li@gmail.com)

consistent [Hajj et al., 2004; Schreiner et al., 2007; Foelsche et al., 2009; Foelsche et al., 2011]. Second, RO measurements can be performed under essentially all-weather conditions and they are available globally. Furthermore, the retrieved atmospheric profiles have a high accuracy and a high vertical resolution in the upper troposphere and lower stratosphere region [e.g., Kursinski et al., 1997; von Engel et al., 2003].

[5] Due to the above mentioned characteristics, RO data have been used to study the Earth's weather and climate. For example, RO data have been used for studying atmospheric dynamics, performing climate monitoring and analyzing trend detection [see Anthes, 2011; Steiner et al., 2011; for reviews]. It has also been demonstrated that the assimilation of RO data in numerical weather prediction (NWP) systems can significantly improve the quality of the forecast products, especially in the polar and oceanic regions [e.g., Healy and Eyre, 2000; Healy and Thépaut, 2006; Cucurull and Derber, 2008; Le Marshall et al., 2010]. In addition, RO data have been successfully used for space weather research [see, e.g., Yue et al., 2010; Anthes, 2011; Carter et al., 2013].

[6] Though the RO technique has been quite successful, the quality of the retrieved bending angles decreases above about 30 km due to the effects of residual ionospheric errors [Bassiri and Hajj, 1993; Vorob'ev and Krasil'nikova, 1994; Ladreiter and Kirchengast, 1996; Syndergaard, 2000; Rocken et al., 2009; Mannucci et al., 2011; Danzer et al., 2013; Liu et al., 2013] and of other remaining observational errors [Kursinski et al., 1997; Steiner and Kirchengast, 2005; Scherllin-Pirscher et al., 2011a]. These errors in bending angle profiles are propagated to refractivity profiles through an Abel integral and are further propagated to other atmospheric profiles through the hydrostatic integral [Rieder and Kirchengast, 2001; Steiner and Kirchengast, 2005]. It is therefore important to carefully initialize the bending angles at high altitudes to minimize these error propagation effects and thereby optimize the climate monitoring utility of the retrieved profiles. Statistical optimization is a commonly used method for this purpose, it combines observed and background bending angles, inversely weighted by their error (co)variance estimates, to determine optimized bending angles [see Ho et al., 2012; Steiner et al., 2013; for an overview on current optimization schemes].

[7] In this study, a new dynamic statistical optimization approach for obtaining better optimized bending angle profiles is presented. Section 2 first briefly reviews existing statistical optimization algorithms and then presents our new approach; section 3 presents and evaluates the results from the new approach, and conclusions are given in section 4.

2. Statistical Optimization

2.1. Existing Algorithms

[8] Statistical optimization was first introduced for RO data processing by Sokolovskiy and Hunt [1996]. This method uses the weighted average of observed bending angles and background bending angles to determine the optimal bending angles, where the weights of the two types of bending angles are determined by their error covariance matrices or by approximations to it (e.g., from ignoring error correlations). The general picture is as follows [e.g., Healy, 2001; Rieder and Kirchengast, 2001; Gobiet et al., 2007]: At high altitudes in the mesosphere (above about 60 km), the background errors are smaller than the observation errors; thus, the background

bending angle contributes more to the optimized bending angle. With decreasing altitude, the background error increases while the observation error stays roughly constant, so that the optimized bending angles smoothly transit from being more weighted toward the background bending angles to being more weighted toward the observed bending angles. In the range below about 40 km, the observed bending angle dominates in the optimized bending angle, due to the higher quality of the observed bending angle.

[9] Given an unbiased background bending angle profile and observed bending angle profile α_b and α_o , respectively, and their error covariance matrices \mathbf{C}_b and \mathbf{C}_o , the statistically optimized bending angle profile α_{SO} can be calculated by [Healy, 2001; Gobiet and Kirchengast, 2004]:

$$\alpha_{SO} = \alpha_b + \mathbf{C}_b(\mathbf{C}_b + \mathbf{C}_o)^{-1} \cdot (\alpha_o - \alpha_b). \quad (1)$$

This method is a generalized least squares approach [Rodgers, 1976, 2000], weighting the bending angles by their inverse covariances. As an illustrative and typical example, the background bending angles can be obtained from a climatological model such as the Mass Spectrometer and Incoherent Scatter Radar (MSIS) model [Hedin, 1991], and the background error covariance matrix by guessing a typical relative standard error of the model and a simple error correlation structure like exponential falloff over about an atmospheric scale height [e.g., Healy, 2001] or just disregarding correlations [e.g., Sokolovskiy and Hunt, 1996; Hocke, 1997]. Similarly, the observation error covariance matrix can be formulated from estimating the observation error at mesospheric altitudes (where the signal is small as noted above) and guessing simple error correlations [e.g., Gobiet and Kirchengast, 2004; Gobiet et al., 2007] or again just ignoring the latter.

[10] The main difficulty of effective statistical optimization is to obtain an accurate error covariance formulation for the background bending angles since this is neither supplied together with common (climatological) models nor is its construction a straightforward task. As a result, Sokolovskiy and Hunt [1996] calculated the statistically optimized bending angles in that pioneering work by neglecting the vertical correlations among the background errors and among the observation errors. Equation (1) can be expressed in this case as an equation of inverse variance weighting,

$$\alpha_{SO,i} = \alpha_{b,i} + \frac{\sigma_{b,i}^2}{\sigma_{b,i}^2 + \sigma_{o,i}^2} (\alpha_{o,i} - \alpha_{b,i}), \quad (2)$$

where $\sigma_{b,i}$ and $\sigma_{o,i}$ are the standard deviations of the background bending angle and the observed bending angle at the i th impact altitude level, respectively. σ_b is estimated as a fixed fraction of α_b and σ_o is empirically estimated as a constant value at mesospheric altitudes, in line with the illustrative example described above.

[11] An alternative approach was adopted by Hocke [1997] and Steiner et al. [1999] for the purpose of down-weighting outliers and smoothing the obtained optimized bending angles at high altitudes:

$$\alpha_{SO,i} = \alpha_{b,i} + \frac{\sigma_{b,i}}{\sigma_{b,i} + \sigma_{o,i}} (\alpha_{o,i} - \alpha_{b,i}). \quad (3)$$

This was found effective for the purpose, but from the viewpoint of unbiased optimal estimation it can be argued that this approach overweighs the background bending angle

if the background error is larger than the observation error, and it also overweighs the observed bending angle if the observation error dominates [Healy, 2001].

[12] Healy [2001] and Rieder and Kirchengast [2001] were the first to suggest and demonstrate the value of using full error covariance matrices for RO statistical optimization, considering this carefully in the framework of optimal estimation methodology [Rodgers, 2000]. We summarize the Healy [2001] formulation here, which focuses on bending angles. As above, the background standard deviations are assumed to be a fixed fraction of the background bending angles and the observation standard deviations are empirically estimated as a constant; however, the correlations are no longer ignored. The background error correlations were expressed by a correlation function of Gaussian shape with a correlation length of 6 km, reflecting the atmospheric scale height. The observation errors were assumed uncorrelated or correlated with a small correlation length (about 1 km, also using a Gaussian shape for the correlation functions). Adopting this, each element of the background error covariance C_b is formulated as

$$C_{b,ij} = \sigma_{b,i}\sigma_{b,j} \exp\left(-\frac{(a_i - a_j)^2}{L^2}\right), \quad (4)$$

where a_i and a_j are the impact parameters at height indices i and j , and L is the background error correlation length. The formulation of the observation error covariance matrix C_o is the same as the formulation of C_b , but with σ_o and a shorter correlation length.

[13] Healy [2001] demonstrated that the background error correlation is important and helpful for smoothing the optimized bending angle profile while keeping it unbiased at the same time. If the background error correlations are neglected, the optimized profile is bounded by the observed and the background profile at each impact altitude level and takes the noisy shape of the observed profile. Regarding the shape of the correlation functions, it subsequently became clear that exponential falloff is of numerical advantage over Gaussian shape, since the former leads to error covariance matrices that are robustly invertible while the inversion of the latter is readily unstable, except if the Gaussian is approximated by a suitable polynomial fit [Steiner and Kirchengast, 2005; section 6 therein].

[14] Gorbunov [2002] introduced an algorithm combining ionospheric correction and statistical optimization. Briefly, this method dynamically estimates signal and noise covariances at individual impact altitude levels; vertical error correlations are not accounted for. The signal covariance is estimated from the differences between the observed bending angle and background bending angle in a height range where the neutral atmospheric signal prevails (i.e., lower stratosphere). The noise covariance is estimated from the bending angles at the two GPS frequencies in the height range where ionospheric signals prevail (i.e., mesosphere). With the estimated signal and ionospheric observation covariances, the neutral atmospheric bending angle (statistically optimized bending angle in our context) could then be optimally estimated and used for the calculation of refractivity. The current retrieval at the RO processing center at Danish Meteorological Institute (DMI) is employing this Gorbunov [2002] approach as part of its statistical optimization [Lauritsen et al., 2011; Ho et al., 2012].

[15] Lohmann [2005] showed that if both observed and background errors were estimated dynamically and the vertical correlation was neglected, the two types of errors are not damped equally when using the Abel transform to calculate refractivity. To mitigate this problem, Lohmann [2005] adjusted the magnitude of the two types of errors using a scaling factor estimated from calculated error correlation lengths of the two types of errors. The current retrieval of the University Corporation for Atmospheric Research (UCAR) RO processing center is employing this Lohmann [2005] approach as part of its statistical optimization [Ho et al., 2012].

[16] Gobiet and Kirchengast [2002] followed the Healy [2001] and Rieder and Kirchengast [2001] approach of using a full error covariance matrix for the statistical optimization. Instead of using a Gaussian-shape function an exponential falloff function was used to estimate the error correlation for both background and observed bending angles. They also used a search for that background bending angle profile in the MSIS model space that best fits the observed profile over the stratopause region. Gobiet and Kirchengast [2004] updated this algorithm by performing an additional bias correction to the background bending angle profile before the statistical optimization, aiming at further minimizing residual biases in the optimized bending angle profile under adverse conditions such as during high-latitude winter. Another improvement by Gobiet et al. [2007] introduced the use of background profiles from European Centre for Medium-range Weather Forecast (ECMWF) fields rather than from the MSIS model (avoiding also the additional bias correction noted above).

[17] The Wegener Center for Climate and Global Change (WEGC) Occultation Processing System version 5.4 (OPSV5.4) [Pirscher, 2010; Ho et al., 2012; Steiner et al., 2013], which is used as reference system for this study, uses colocated bending angle profiles extracted from ECMWF short-range (24 h/30 h) forecast fields as background profiles. Its statistical optimization is otherwise following Gobiet et al. [2007], as recently summarized by Ho et al. [2012]. The ECMWF forecast fields are used at horizontal resolution T42 (spectral representation with triangular truncation at wave number 42), corresponding to about 300 km, for roughly matching the horizontal resolution of RO data. We use this OPSV5.4 algorithm as evaluation reference, since it is amongst the major RO processing centers currently the only one employing statistical optimization with full covariance matrices [cf. algorithm descriptions by Ho et al., 2012] and since recent intercomparison results indicate that this is a performance advantage above about 20 km [Ho et al., 2012; Steiner et al., 2013]. We therefore consider that we compare to a current state-of-the-art algorithm so that any evidence of further improvement that we may find is expected to improve also other existing algorithms.

[18] Recently, Ao et al. [2012] and Gleisner and Healy [2013] introduced an alternative high altitude initialization method that can be used for preparing refractivity and atmospheric profile climatologies without first retrieving individual profiles that require statistical optimization with background profiles. The method first produces averaged-observed bending angle profiles to effectively mitigate random noise at high altitudes, that is climatological bending angle profiles are first generated, from which climatological refractivity and atmospheric profiles can then be retrieved without

further initialization. The relative quality of these climatologies, compared to climatologies averaged from individual-profile retrievals that included initialization by statistical optimization, will depend on the data quality (i.e., will be different for different RO receivers such as on CHAMP, COSMIC, and MetOp-A), the suitability of the data quality-control and averaging scheme used, and the space-time-averaging domain trade-offs involved. Moreover, it will depend on the quality of the background profiles and the performance of the statistical optimization scheme used for the individual-profile retrievals providing the comparative results.

[19] The new dynamic optimization approach that we introduce in this study does not look at these two avenues as a competition but rather exploits their synergy and combines them: averaged-observed bending angle profiles are integral part of background bending angle estimation and their weight in resulting background profiles will depend on the uncertainties estimated for these averaged-observed profiles relative to those estimated for averaged-analysis profiles determined from ECMWF fields. The approach is described in detail in the following subsections.

2.2. The New Dynamic Approach

[20] As can be seen from equation (1), the critical part for effective statistical optimization is to obtain accurate background profiles and associated background error covariance matrices, alongside with adequate observation error covariance matrices. Due to the high correlation amongst the background errors at different heights, neglecting this correlation or using just a crude formulation of background error covariance matrices will degrade the quality of the optimized bending angles [Healy, 2001]. The existing schemes summarized above share this weakness of crude formulation. Therefore, the main focus of this study is to introduce a new dynamic method for obtaining more adequate background bending angles and error covariance matrices, based on ensembles of background bending angle profiles extracted from ECMWF short-range forecast and analysis fields as well as of observed bending angle profiles. Including dynamic estimation also of observation error covariance matrices similar to the background ones here is left as part of a follow-on study that also evaluates the new approach on large (full month) data sets. The primary advance is expected to come from the improved background formulation introduced here.

[21] Figure 1 illustrates the algorithmic steps of the new method, sequentially including the three major steps of 1) constructing the basic daily background fields for any day to be processed, 2) preparing the derived daily background fields with the specific statistical quantities directly needed for the statistical optimization, and 3) performing the actual dynamic statistical optimization for all RO events of any given day. We describe the method along this three-step sequence, explaining along the way also the component tasks indicated in Figure 1.

2.2.1. Construction of Basic Daily Background Fields

[22] In order to suitably capture the large-scale background error dynamics as a function of latitude, longitude, (impact) altitude, and time, we prepare once-daily fields of all basic background variables needed, globally at a 10° latitude \times 20° longitude grid (center of base cell/anchor gridpoint at 5°N , 10°E), at

200 representative (impact) altitude levels from 0.1 km to 80 km. This yields daily fields at a global $18 \times 18 \times 200$ grid.

[23] The basic statistical variables that are needed for the dynamic method in form of such gridded fields—which we prepared into daily data files for easy use for processing all RO events of a day—include: (i) the mean analysis bending angle from the ensemble of analysis values for any grid point (i.e., any of the 200 levels in each of the 18×18 cells) $\bar{\alpha}_a$, (ii) the analysis spread (standard deviation of the ensemble of analysis values) against this mean s_a , (iii) the estimated bias (systematic uncertainty) of this mean b_a , (iv) the mean forecast bending angle $\bar{\alpha}_f$, (v) the standard deviation of the forecast values against this mean s_f , (vi) the standard deviation of the forecast-minus-analysis difference profiles for any grid point s_{f-a} , (vii) the number of values in the analysis and the forecast ensemble for any grid point $N_{a,f}$, (viii) the error correlation matrix (200×200 correlation values) estimated from the forecast-minus-analysis difference profiles over the entire globe \mathbf{R}_{f-a} , (ix) the mean observed bending angle from the ensemble of observed values for any grid point $\bar{\alpha}_o$, (x) the standard deviation of the observed values against this mean s_o , (xi) the estimated bias (systematic uncertainty) of this mean b_o , (xii) the mean colocated bending angle $\bar{\alpha}_c$, (xiii) the standard deviation of the colocated values against this mean s_c , and (xiv) the number of values in the observed and the colocated ensemble for any grid point $N_{o,c}$.

[24] In constructing these basic variables on the daily $18 \times 18 \times 200$ grids, we apply time-averaging over at least five days (from two days before to two days after the day of interest) and horizontal-averaging over geographic domains of at least $1000 \text{ km} \times 1000 \text{ km}$ size (over 10° lat \times 20° lon cells out to $60^\circ\text{S}/60^\circ\text{N}$ latitude, poleward over larger longitude ranges of 25° from 60° to 70° , 40° from 70° to 80° , 90° from 80° to 90° latitude); only the daily background error correlation matrix is constructed from horizontal-averaging over the entire globe (yielding a robust estimation of the 200×200 correlation values, i.e., of the 200 vertical correlation functions of all 200 altitude levels).

[25] This construction approach, and the degree of averaging applied, was proven by extensive sensitivity tests with different time- and space averages (more and less days, larger and smaller horizontal domains, etc.) and found to be just adequate so that the variables in the resulting fields have essentially averaged-out all weather variability (at scales of up to several days and including all mesoscale-sized systems) but still neatly trace all weekly to climate-scale variations and large-scale geographic variation patterns. The sensitivity tests also proved that the averaging is robust (sufficiently large number of ensemble members in the average) and not sensitive to the exact choices of time period and geographic size as long as at least about 5 days and 1000 km scale sizes are utilized (e.g., 5 days to 7 days and 1000 km to 2000 km horizontal scale sizes not making much difference; if options of even stronger averaging are used, like up to monthly means, some important weekly scale structures, like from sudden stratospheric warming events as an arbitrary example, are no longer traced by the estimated mean fields). In other words, the averaging decides on the trade-off between what is considered mean-field variation, which should be dynamically traced by the background error formulation to enable to be as unbiased as possible in a statistical sense, and what is considered weather variability, the quasi-random

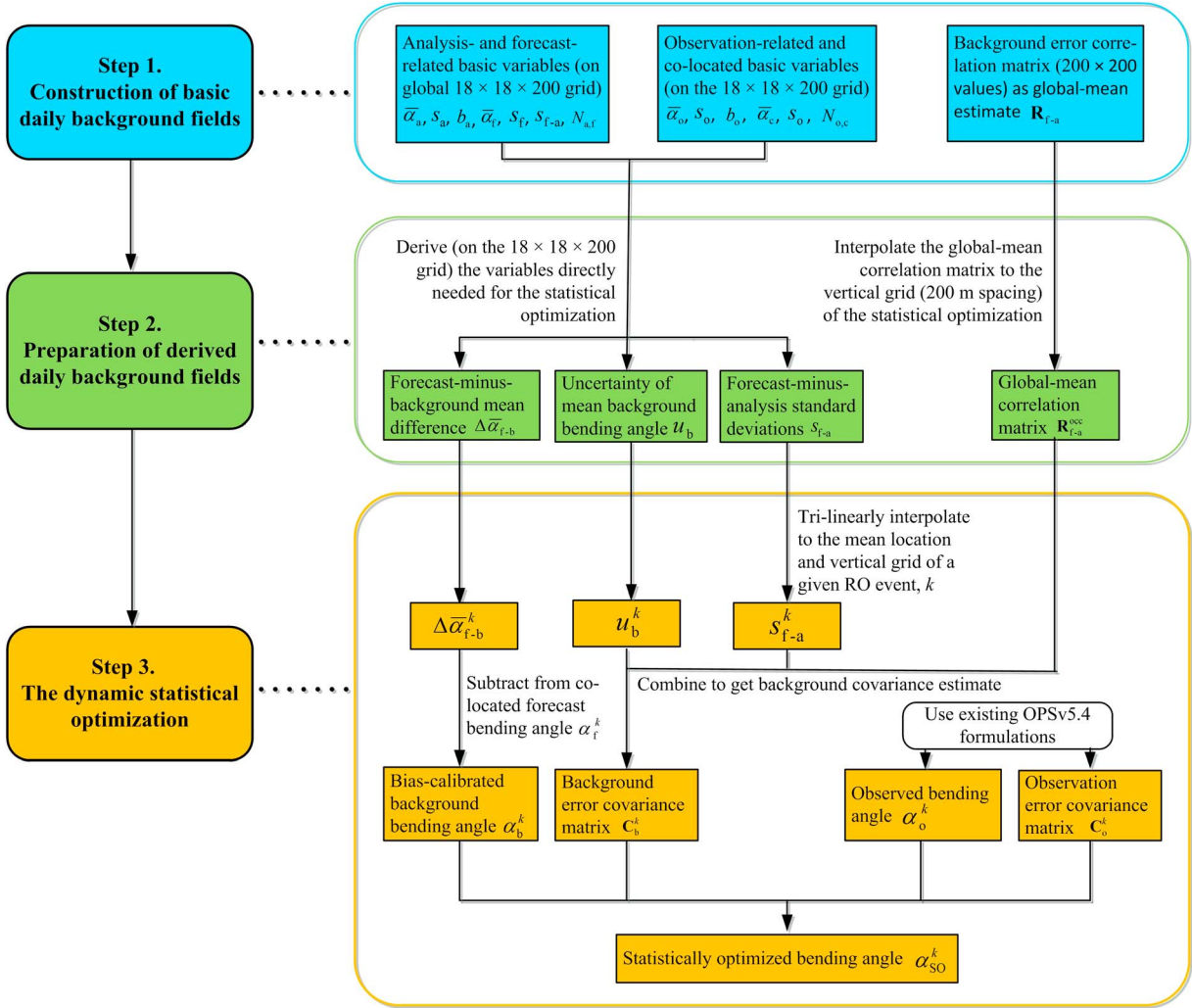


Figure 1. Schematic illustration of the algorithmic steps of the new statistical optimization approach; for description see section 2.2.

variation of individual RO profiles in the sense of a spread, or standard deviation around the mean.

[26] We used ECMWF analysis fields and corresponding 24 h-forecast fields at T42L91 resolution (about 2.8° lat \times 2.8° lon, 91 hybrid-pressure vertical levels up to about 80 km), at 00 UTC and 12 UTC each day, as the basis to construct the $18 \times 18 \times 200$ gridded fields of analysis and forecast variables. On the observation side, we used observed RO bending angle profiles mainly from Formosat-3/COSMIC that were obtained from Wegener Center OPSv5.4 processing on the basis of excess phase and orbit data obtained from UCAR/CDAAC. These OPSv5.4 RO profiles come with colocated ECMWF analysis profiles that we also co-use here for estimating and taking into account the sampling error [Scherrlin-Pirscher et al., 2011b]. The approach is generic, however, and any other source of analysis and short-range forecast fields and observed bending angle profiles could be used as well. We chose ECMWF and WEGC-OPS for their proven track records of data sets of leading quality [e.g., Untch et al., 2006; Scherrlin-Pirscher et al., 2011a, 2011b; Ho et al., 2009, 2012; Steiner et al., 2013]. As an alternative to the ECMWF operational fields, we also consider the use

of the analysis and forecast fields from the ERA-Interim reprocessing [Simmons et al., 2007; Dee et al., 2011].

[27] The 200 level vertical grid was defined to safely accommodate different analysis/forecast level schemes up to fine ones, such as ECMWF’s level schemes from L60 (before February 2006) to L137 (from June 2013), but still keeping the level number reasonably small for the sake of efficient data storage, considering these daily grid fields will be needed over years of climate data processing. Practically, the level spacing that we found useful and therefore adopted is: 100 m below 1 km, then linearly increasing from 100 m at 1 km to 600 m near 60 km, furthermore to 1000 m at 70 km, then kept constant at 1000 m up to 80 km.

[28] The fundamental ensemble of bending angle profiles for statistically computing all the analysis and forecast variables for each of the 18×18 cells was extracted from the ECMWF T42L91 fields on a $2.5^\circ \times 2.5^\circ$ native grid, for the 10 UTC time layers of five days, and at the 200 target levels. This yields an ensemble of many hundreds of profiles per cell (and many thousands globally for the correlation matrix), which allows robust estimates of the statistical variables. The GCM Atmosphere Model (GCMAtm) of the Wegener

Center OPS software was used for this purpose. The bending angle is derived in the GCMAtm by forward Abelian transformation from refractivity which in turn is derived from the variables pressure, temperature, and humidity by Smith-Weintraub's refractivity equation.

[29] The ensemble of observed bending angle profiles, and of their collocated analysis profiles, is simply adopted to consist of all RO events that fall into each cell over the five days, which typically leads to approximately 40 RO events per cell. In general, should observed-profile ensemble sizes be considered too small, for example during time periods before mid-2006 where mainly the CHAMP satellite provided RO data, the averaging domain can be enlarged (primarily along longitude, secondarily in the number of days). More details of how the statistical variables were computed are separately described in section 2.3.

2.2.2. Preparation of Derived Daily Background Fields

[30] Using the basic background fields—read in from the applicable daily data file before processing the RO events of a day—we prepared those specific statistical quantities on the $18 \times 18 \times 200$ grid that are directly needed in the statistical optimization processing of the RO events of the day. These include (i) the forecast-minus-analysis standard deviation s_{f-a} , which represents the estimated random uncertainty of the 24 h-forecasts and can be adopted as is, (ii) the mean background bending angle $\bar{\alpha}_b$, which is an optimally estimated combination of $\bar{\alpha}_a$ and $\bar{\alpha}_o$ and where we actually use the difference of the forecast mean to the background mean $\Delta\bar{\alpha}_{f-b}$, and (iii) the estimated combined standard uncertainty of the background mean u_b , respectively.

[31] The background mean $\bar{\alpha}_b$, its associated uncertainty u_b , and the forecast-minus-background mean difference $\Delta\bar{\alpha}_{f-b}$ are computed using standard equations for variance-based uncertainty propagation and for inverse-variance weighting as follows,

$$\bar{\alpha}_b = \frac{u_o^2}{u_o^2 + u_a^2} \bar{\alpha}_a + \frac{u_a^2}{u_a^2 + u_o^2} [\bar{\alpha}_o - (\bar{\alpha}_c - \bar{\alpha}_a)], \quad (5)$$

$$u_b = \left[\frac{u_a^2 u_o^2}{u_a^2 + u_o^2} \right]^{1/2}, \quad (6)$$

$$\Delta\bar{\alpha}_{f-b} = \bar{\alpha}_f - \bar{\alpha}_b, \quad (7)$$

where

$$u_a = [b_a^2 + (s_a^2/N_{a,f})]^{1/2} \quad (8)$$

and

$$u_o = [b_o^2 + (s_o^2/N_{o,c}) + r_{\text{resSE}}^2 (\bar{\alpha}_c - \bar{\alpha}_a)^2]^{1/2} \quad (9)$$

are the estimated combined standard uncertainties of the mean analysis bending angle and the mean observed bending angle, respectively. The third term on the right-hand side of equation (9) is the residual sampling error estimate for the RO observations [Scherrlin-Pirscher *et al.*, 2011b], where we set the reduction factor r_{resSE} to 0.3 following the (conservative) empirical estimate by Scherrlin-Pirscher *et al.* [2011b]. Due to the large ensembles with fairly high numbers of profiles per grid cell, the bias terms (b_a and b_o terms)

generally dominate in equations (8) and (9) so that the resulting background mean uncertainty u_b (equation (6)) represents essentially a bias-type (systematic) uncertainty. Further discussion of these estimates follows in section 3.

[32] Equations (5) to (9) are applied grid point wise to the entire $18 \times 18 \times 200$ grid so that the quantities needed for the statistical optimization, $\Delta\bar{\alpha}_{f-b}$, u_b , and s_{f-a} , are conveniently available in form of this global grid for interpolation to any RO event location occurring during the day.

[33] Completing this once-daily preparation of variables, the error correlation matrix of the day, \mathbf{R}_{f-a} , is interpolated from its 200-level formulation to the target vertical grid of the statistical optimization. For the latter, we chose a 200 m equidistant grid, with 400 levels from 0.2 km to 80 km, so that this yields a correlation matrix with up to 400×400 values (in this study, we apply statistical optimization down to 30 km only, corresponding to 251×251 values). We performed the interpolation linearly along the diagonal and parallels to the diagonal (at the top and bottom boundaries linearly along the boundaries) in order to accurately conserve the shape of the matrix. The resulting matrix $\mathbf{R}_{f-a}^{\text{occ}}$ is robustly invertible and can now be used for all RO events of the day; further details are given in section 2.3.

2.2.3. The Dynamic Statistical Optimization

[34] For each occultation event k , assuming $k=1, \dots, N_{\text{occ}}$ being sequentially numbered RO events of the day, we first determine the collocated profiles $\Delta\bar{\alpha}_{f-b}^k$, u_b^k , and s_{f-a}^k from the respective grids $\Delta\bar{\alpha}_{f-b}$, u_b , and s_{f-a} by bilinear latitude/longitude interpolation to the RO event location and linear vertical interpolation to the (200 m spacing, 400 level) target grid of the statistical optimization. We also employ the correlation matrix $\mathbf{R}_{f-a}^{\text{occ}} = R_{f-a,ij}^{\text{occ}}$ for each event k , to represent its background error correlations.

[35] Adopting now the general optimal estimation scheme of equation (1), we cast the computation of the statistically optimized bending angle α_{SO}^k into the form

$$\alpha_{\text{SO}}^k = \alpha_b^k + \mathbf{C}_b^k (\mathbf{C}_b^k + \mathbf{C}_o^k)^{-1} \cdot (\alpha_f^k - \alpha_b^k), \quad (10)$$

where

$$\alpha_b^k = \alpha_f^k - \Delta\bar{\alpha}_{f-b}^k \quad (11)$$

is the collocated background bending angle, computed by subtracting the forecast-minus-background mean difference $\Delta\bar{\alpha}_{f-b}^k$ from the collocated forecast bending angle α_f^k in order to effectively reduce the residual bias in α_b^k to within the estimated uncertainty of the background mean u_b^k (otherwise, as in the existing OPSv5.4 scheme, potential biases in α_f^k would survive). The background error covariance matrix $\mathbf{C}_b^k = C_{b,ij}^k$ is formulated as

$$C_{b,ij}^k = u_{b,i}^{\text{occ}} \cdot u_{b,j}^{\text{occ}} \cdot R_{f-a,ij}^{\text{occ}}, \quad (12)$$

where the combined standard uncertainty profile u_b^{occ} , determining the diagonal variances ($u_{b,i}^{\text{occ}} \cdot u_{b,i}^{\text{occ}} \cdot 1$) and the off-diagonal covariance elements of \mathbf{C}_b^k , is estimated as

$$u_b^{\text{occ}} = \left[\left(f_{\text{bcvg}} \cdot u_b^k \right)^2 + \left(s_{f-a}^k \right)^2 \right]^{1/2}. \quad (13)$$

[36] Herein we employ the bias coverage factor f_{bcvg} to strongly penalize the estimated bias-type uncertainty u_b^k

(cf. equations (5) to (9)) relative to the estimated random uncertainty s_{f-a}^k , in order to minimize the influence from potential residual background biases on the resulting optimized profile α_{SO}^k (in this study $f_{bcvg} = 5$, for more discussion see section 3). The bending angle observation error covariance matrix, \mathbf{C}_o^k , is modeled in this study in the same way as in the existing OPSv5.4 scheme [Ho et al., 2012; Steiner et al., 2013]. A brief summary of the formulation is given in subsection 2.4; advancing it in a similar way as \mathbf{C}_b^k is part of ongoing work. The observed bending angle itself, α_o^k , is as well used as provided by the OPSv5.4 bending angle retrieval.

[37] Taking an overall look at this new dynamic scheme, we may summarize the following key advancements over existing schemes: 1) we use a 3D- and time-dependent formulation of all key statistical variables needed in the formulation of \mathbf{C}_b^k , based on reliable ensembles of atmospheric ECMWF forecast and analysis profiles as well as of observed RO profiles, while existing formulations use globally static relative errors and either climatologies (still most common; see section 2.1) or forecasts (OPSv5.4), or observations (climatological profile retrievals only; see section 2.1); 2) we use a bias estimate $\Delta\bar{\alpha}_{f-b}^k$, allowing to reduce the bias in the colocated background profile α_b^k , while existing schemes use no such bias mitigation measure; 3) we use estimates of background bias uncertainty u_b^k and random uncertainty s_{f-a}^k , and penalize u_b^k against s_{f-a}^k to minimize bias influence on α_{SO}^k , while existing schemes use globally static relative background errors (see section 2.1); 4) we use daily updated realistic empirical estimates of background error correlations, \mathbf{R}_{f-a}^{occ} , while existing schemes either ignore these correlations or use crude (exponential) falloff models not representing realistic correlation shapes.

[38] Furthermore, equations (6), (8), and (9) show that the dynamic method is flexible in a seamless manner to either include $(\bar{\alpha}_a, u_a)$ or $(\bar{\alpha}_o, u_o)$ or both of them in the formulation of background bias estimation $(\Delta\bar{\alpha}_{f-b}, u_b)$, so that users of the method can readily decide what to include according to their context and preferences. Also, the grid definition, and the space- and time-averaging domains per grid cell, can be flexibly adjusted by users. Based on all these advantages, we expect the new method to outperform existing schemes; section 3 provides intercomparisons to the OPSv5.4 scheme.

2.3. Estimation of the Variables for the Background Error Covariance Matrix

[39] This subsection complements the above introduction of the new method by providing more details on the computation of the key variables for constructing \mathbf{C}_b^k , discussing 1) the estimation of the analysis- and forecast-related variables $\bar{\alpha}_a$, s_a , $\bar{\alpha}_f$, s_f , s_{f-a} , and \mathbf{R}_{f-a} , 2) the estimation of the analysis bias b_a , and 3) the estimation of the observation-related variables $\bar{\alpha}_o$, s_o , b_o , and of their associated colocated variables $\bar{\alpha}_c$ and s_c .

2.3.1. Estimation of Analysis- and Forecast-Related Variables

[40] The first step is to extract the analysis and forecast bending angle profiles from the respective ECMWF T42L91 fields on a regular $2.5^\circ \times 2.5^\circ$ horizontal grid, which is comparable to the horizontal resolution of the ECMWF T42 fields. We used 10° latitude \times 20° longitude cells (more longitude extent poleward of 60° , compensating for the meridian convergence) and five days of ECMWF data

(containing 10 time layers, five each 00 UTC and 12 UTC), as summarized in section 2.2.

[41] As a result, in each of the $10^\circ \times 20^\circ$ cells, there are 320 analysis profiles and 320 forecast profiles (more poleward of 60°) that were used to calculate the mean profiles, $\bar{\alpha}_a$ and $\bar{\alpha}_f$, and their standard deviations, s_a and s_f , using standard estimation equations [e.g., Steiner and Kirchengast, 2004]. The calculations of s_{f-a} and \mathbf{R}_{f-a} for each cell use the differences between the forecast and analysis bending angles of all the 320 pairs of profiles, also following standard estimation equations [Steiner and Kirchengast, 2004].

[42] The global-mean correlation matrix \mathbf{R}_{f-a} is finally calculated by averaging the individual correlation matrices of all $10^\circ \times 20^\circ$ cells. While the individual matrices per cell appear still noisy in shape, this global averaging effectively draws from an ensemble of more than 100,000 native profiles ($320 \times 18 \times 18$), providing a very robust estimation. Based on our extensive testing, we found that the correlation lengths of main peaks and the shape of the correlation functions depend little on latitude and longitude so the averaging is well justified. As seen in equations (12) and (13), we then use \mathbf{R}_{f-a} as the correlation matrix for the full matrix \mathbf{C}_b^k , including both the bias-type uncertainty u_b^k and the random uncertainty s_{f-a}^k , although by construction \mathbf{R}_{f-a} only represents the correlation of the errors expressed by s_{f-a}^k . While one could include some rough guess of long-range correlation also for the bias-type errors expressed by u_b^k , which are dominated by the analysis and observation biases b_a and b_o (cf. equations (8) and (9)), we considered this not needed since these correlations are quantitatively unknown and the results are quite reasonable with just using \mathbf{R}_{f-a} .

[43] Figure 2 shows the variation of the relative forecast-minus-analysis standard deviations, $100 \cdot (s_{f-a}^k / \bar{\alpha}_a)$ [%], on two example days (15 January and 15 July 2008), which represent winter in the northern and southern hemispheres, respectively. It shows that large values of standard deviation occur in the winter hemisphere at high latitudes. In the Arctic and Antarctic winter, the relative standard deviations are larger than 10% at 80 km impact altitude, decreasing to $\sim 5\%$ at 70 km, $\sim 3\%$ at 50 km, and to $\sim 1\%$ below 25 km. In the nonpolar regions, the values amount approximately to 3% to 4% near 80 km and to 1% to 2% below. This reflects that the ECMWF 24 h-forecast errors (at T42L91 resolution) are in general fairly small, much smaller than the uncertainties that typically need to be assumed for climatologies (15% to 20%).

[44] Furthermore, in course of testing, we found the s_{f-a}^k estimates consistent with flow-dependent forecast error estimates produced by ECMWF's ensemble of data assimilations (EDA) system [M. Bonavita, ECMWF, pers. communications, 2012; Bonavita et al., 2011; Isaksen et al., 2010]. s_{f-a}^k is a reasonable estimator for our purpose also in the sense that it provides a tentatively conservative estimate of random forecast errors, due to its construction from forecast and analysis differences, which include as well random analysis errors (being generally a minor contribution compared to the forecast errors, though).

[45] Figure 3 illustrates exemplary error correlation functions extracted from \mathbf{R}_{f-a} , for three representative altitude levels (30 km, 50 km, 70 km), as well as the correlation length of the correlation functions for all the 200 altitude levels (only altitude levels within 20 km to 80 km are shown). It can be seen in the left panel that the correlation functions

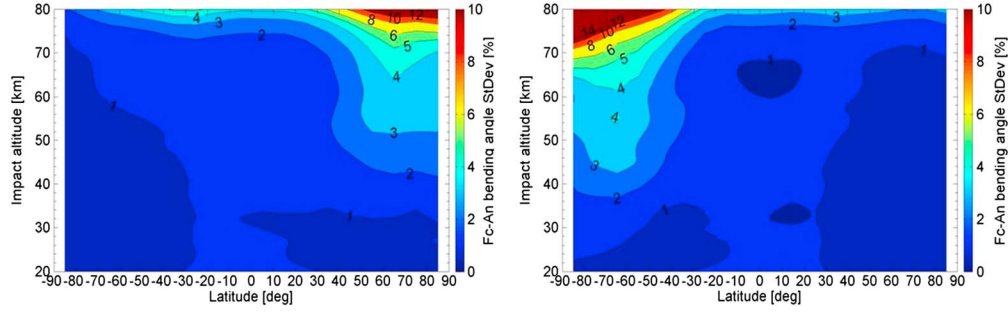


Figure 2. Relative standard deviations of forecast-minus-analysis bending angle differences as function of latitude (10° bins, zonal means) and impact altitude (200 level grid) on 15 January 2008 (left panel) and 15 July 2008 (right panel).

have a near-Gaussian shape at the main peak (confirmed by fitting tests), which denotes high correlation close to the main peak (where the correlation is unity by definition) and a relatively sharp correlation decrease outward. Outside of the main peak, there are next two somewhat asymmetric negative side peaks, which denotes anticorrelation of the errors at these altitude levels to the error at the main peak. Further out from the negative peaks, the correlations gradually decrease to zero in the far range from the main peak. The right panel shows the variation in the error correlation length, ranging from about 0.8 km to 6 km in the impact altitude range from 20 km to 80 km. The background error correlation length assumed in the OPSv5.4 is comparatively broader [10 km throughout; e.g., *Steiner et al.*, 2013].

2.3.2. Estimation of the Analysis Bias

[46] The relative bias in the ECMWF analysis bending angles, $100 \cdot (b_a / \bar{a}_a)$ [%], is propagated from an estimated analysis temperature bias $b_{a,T}$. Since we know \bar{a}_a , we can then determine b_a from the relative bias. Due to lack of robust knowledge and associated lack of robust quantification capability for the analysis bias, because the “true” state is hard to know (M. Bonavita and S. B. Healy, ECMWF, pers. communications, 2012), we formulated $b_{a,T}$ as a simple analytical model with dependencies on altitude, latitude, and season (day of year). The structure of the model largely follows the empirical-analytical error model of *Scherllin-Pirscher et al.* [2011b], equations (2) to (6) therein.

[47] The selection of the model’s fitting parameters and the selected structure of the model is based on discussions with ECMWF (M. Bonavita, pers. communications, 2012) and on related ECMWF experience from intercomparison with various analysis/forecast systems from other weather centers and against nonbias-corrected reference data such as radiosondes and RO data. A particular difficulty limiting detailed knowledge on $b_{a,T}$ is that accurate reference data above about 35 km (over the upper stratosphere and mesosphere) are sparse, calling for conservative estimation.

[48] The vertical structure of the model is slightly simplified compared to *Scherllin-Pirscher et al.* [2011b], equation (2) therein, and constructed in the following way: below the bottom of the upper stratosphere z_{USbot} , a small constant value of s_0 is set to be the bias, while above z_{USbot} , the bias is set to increase linearly with altitude:

$$b_{a,T} = \begin{cases} s_0 & \text{for } z_{\text{surf}} < z \leq z_{\text{USbot}} \\ s_0 + k_0(z - z_{\text{USbot}}) & \text{for } z_{\text{USbot}} < z < z_{\text{top}} \end{cases} \quad (14)$$

In equation (14), $z_{\text{surf}} = 0.1$ km and $z_{\text{top}} = 80$ km are the bottom and the top level altitudes of the 200 vertical levels defined in section 2.2; z_{USbot} is set to 30 km; and s_0 and k_0 are modeled as functions of latitude and season according to *Scherllin-Pirscher et al.* [2011b], equations (3) to (6) therein (modeling the time parameter τ in day-of-year form).

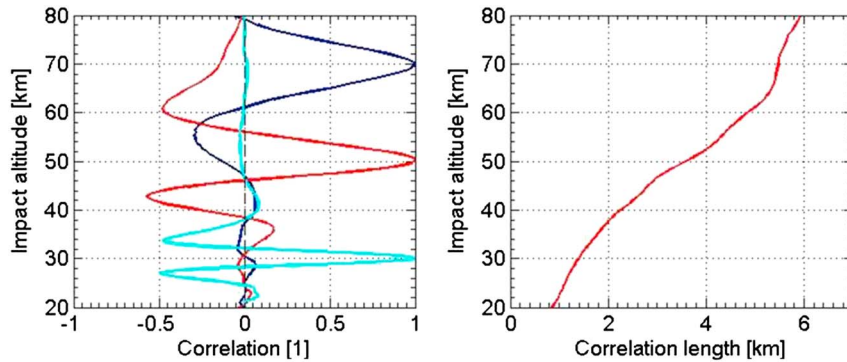


Figure 3. Global mean error correlation functions for three representative impact altitude levels (30 km, 50 km, and 70 km; left panel), and estimated correlation length of the correlation functions at all impact altitude levels from 20 km to 80 km (right panel), for 15 July 2008.

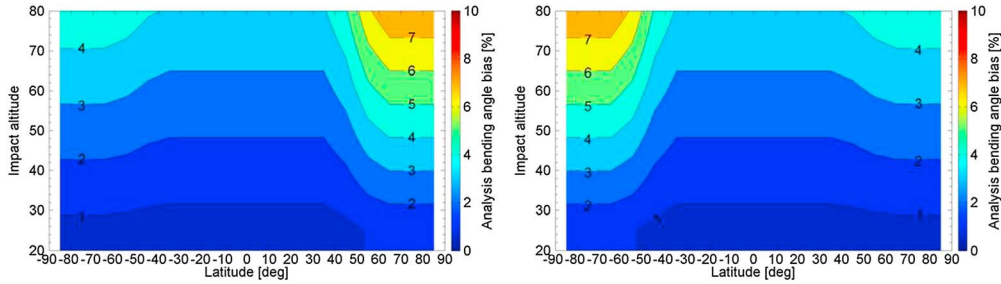


Figure 4. Estimated relative biases, based on simple analytical modeling, for ECMWF analysis bending angles as function of latitude and impact altitude on 15 January 2008 (left panel) and 15 July 2008 (right panel).

We set the basic mean magnitude parameter x_0 to 0.5 K and 0.05 K/km for s_0 and k_0 , respectively, and the maximum amplitude parameter Δx to $0.6x_0$ for both parameters; the factors $f_{\Delta x_0}$ and $f_{\Delta x_s}$, for which values between zero and unity can be adopted, denote the fraction of Δx allocated to latitudinal change and seasonal variations, respectively, and they are set to 1.0 and 0.67 in this study. The parameters $\varphi_{\Delta x_{lo}}$ and $\varphi_{\Delta x_{hi}}$ are the lower and upper latitude boundaries for ensuring that the value of the latitude-dependence function $f(\varphi)$ is zero in the latitude range from the equator to $\varphi_{\Delta x_{lo}}$, linearly increasing from 0 to 1 in the latitude range from $\varphi_{\Delta x_{lo}}$ to $\varphi_{\Delta x_{hi}}$, and remaining 1 from $\varphi_{\Delta x_{hi}}$ to the poles; $\varphi_{\Delta x_{lo}}$ is set to 40° , which is more conservative than 50° that was used by *Scherllin-Pirscher et al.* [2011b]; $\varphi_{\Delta x_{hi}}$ is set to 60° .

[49] These settings ensure that, poleward of 60° , s_0 and k_0 are 20% higher than their basic mean magnitude in the summer hemisphere but twice their mean magnitude in the winter hemisphere. The temperature biases are smallest within the $\pm 40^\circ$ latitude band and at altitudes below 30 km, where the values are equal to the basic mean magnitude of s_0 (0.5 K). The basic setting of k_0 enforces a 0.5 K per 10 km altitude increase of the bias from 30 km upward.

[50] After temperature biases are obtained, the relative bending angle biases are calculated using empirically derived conversion factors from temperature to bending angle. *Scherllin-Pirscher et al.* [2011a] estimated the conversion factor for mapping from temperature errors to relative refractivity errors as $c_{T2N} = 0.5\%/K$, and the conversion factor from relative refractivity to relative bending angle error as $c_{N2\alpha} = 2.4\%/%$; these two factors together resulting in a conversion factor from temperature errors to relative bending angle errors of $c_{T2\alpha} = c_{T2N} \cdot c_{N2\alpha} = 1.2\%/K$. Since use of these conversion factors is well sufficient for our simple model, we adopt this result and compute the relative bending angle bias in the form $100 \cdot (b_a / \bar{\alpha}_a) = c_{T2\alpha} \cdot b_{a,T}$ and in turn invoke $\bar{\alpha}_a$ to finally obtain the estimated bending angle bias b_a .

[51] Figure 4 illustrates the vertical structure of $100 \cdot (b_a / \bar{\alpha}_a)$ for the same two example days as used for illustrating $100 \cdot (s_f - a / \bar{\alpha}_a)$ in Figure 2. The bending angle biases reveal a clear dependence on altitude, latitude, and season, in line with the simple model adopted. For example, at any given altitude level, the bending angle biases within $\pm 40^\circ$ latitude are constant. This reflects the basic magnitude of the biases at each height level and it amounts approximately to 3.5% at 80 km and decreases linearly to about 1% at 30 km. The biases increase poleward from 40° latitude, with a larger increase in the winter hemisphere. The largest biases occur in the polar

winter region where they reach roughly 4% to 8% in the mesosphere, reflecting that these are the most challenging conditions for the ECMWF analyses to provide accurate data.

2.3.3. Estimation of the Observation-Related and Colocated Variables

[52] The mean observed bending angle profile for each cell is calculated using those RO measurements from COSMIC, GRACE, and MetOp-A missions that are located in the cell's domain and that are acquired during the same five days as used for estimating the analysis- and forecast-related variables (test days from January 2008 and July 2008 used in this study; see the results in section 3).

[53] For all satellites, we use excess phase and orbit information provided by UCAR/CDAAC and calculate ionosphere corrected bending angles using an advanced version of OPSv5.4. Since the mean bending angle can be strongly affected by outlier profiles and since we do not apply the whole OPSv5.4 quality control mechanisms (we stop computations at bending angle level and do not check consistency of RO refractivity and temperature profiles by comparing them to reference profiles provided by ECMWF), we apply an additional twofold quality control approach to individual bending angle profiles according to *Foelsche and Scherllin-Pirscher* [2012]: we check individual bending angle profiles in the impact altitude range from 50 km to 80 km and exclude profiles if they have bending angles larger than $40 \mu\text{rad}$ or smaller than $-40 \mu\text{rad}$. Furthermore, we reject all profiles that have bending angles outside of four standard deviations from the mean in the entire impact altitude range.

[54] The mean observed bending angle profiles $\bar{\alpha}_o$ are finally calculated from averaging over all profiles that passed the quality checks; mean colocated bending angle profiles $\bar{\alpha}_c$ are obtained from averaging over the corresponding ECMWF analysis bending angle profiles colocated to the RO events. Their associated standard deviation estimates, s_o and s_c , are computed from the ensemble of observed and colocated profiles, respectively, by the same standard estimation equations as used for s_a and s_f [e.g., *Steiner and Kirchengast*, 2004].

[55] The bias of the mean observed profiles, b_o , is estimated to amount to $0.2 \mu\text{rad}$, based on experience with analysis and intercomparison of bending angle data at high altitudes from different RO satellites, analyses and forecasts, and climatologies. This educated-guess value of $0.2 \mu\text{rad}$ includes errors due to the incomplete removal of the ionospheric contribution to the measurement, multipath errors, errors in the satellite's orbits and velocities, as well as clock bias estimates.

2.4. Formulation of the Observation Error Covariance Matrix

[56] As mentioned in section 2.2, the bending angle observation error covariance matrix \mathbf{C}_o is used in this study in its existing OPSv5.4 form [Ho *et al.*, 2012; Steiner *et al.*, 2013]. Its formulation is therefore, for clarity, just briefly summarized. $\mathbf{C}_o = C_{o,ij}$ is modeled using an estimated observation uncertainty and an exponential-falloff correlation model as:

$$C_{o,ij} = u_{o,i}^{\text{occ}} \cdot u_{o,j}^{\text{occ}} \cdot \exp\left[-\frac{|a_i - a_j|}{L}\right], \quad (15)$$

where a_i and a_j are the impact parameters at i th and j th levels, respectively, and L is the correlation length which is set to 2 km. u_o^{occ} is the observation uncertainty, with the same value used at all altitude levels, which is basically estimated as the standard deviation of the observed bending angle relative to the bias-corrected MSIS bending angle profile at the impact altitude levels from 65 km to 80 km [or to top of profile if reached lower than 80 km; for details on the relevant OPSv5.4 quality control see Pirscher, 2010]:

$$u_o^{\text{occ}} = \sqrt{\frac{1}{|k_{\text{top}} - k_{65}|} \sum_{i=k_{65}}^{k_{\text{top}}} [\alpha_{\text{RO},i} - (\alpha_{\text{MSIS},i} + \beta_o)]^2}. \quad (16)$$

Herein k_{top} and k_{65} are the impact altitude indices for top altitude (nominally 80 km) and 65 km, respectively, and the bending angle bias β_o is estimated by averaging the differences between the RO bending angle α_{RO} and the MSIS-derived bending angle α_{MSIS} in the impact altitude range from 65 km to top (nominally 80 km):

$$\beta_o = \frac{1}{|k_{\text{top}} - k_{65}| + 1} \sum_{i=k_{65}}^{k_{\text{top}}} (\alpha_{\text{RO},i} - \alpha_{\text{MSIS},i}). \quad (17)$$

Equation (16) cannot always reflect the real quality of RO bending angle measurements [Gobiet *et al.*, 2007; Pirscher, 2010]. For such cases, the estimated observation uncertainty u_o^{occ} is modified according to additional quality checks. A detailed description of the OPSv5.4 bending angle retrieval and its statistical optimization is found in Pirscher [2010].

3. Results and Discussion

3.1. Data Sets for the Performance Evaluation

[57] The End-to-End GNSS Occultation Performance Simulation and Processing System (EGOPS) software version v5.5 [Fritzer *et al.*, 2011] was used for both generating simulating MetOp-A data and for retrieving atmospheric profiles from the simulated and real observed RO events. We note that the OPSv5.4 statistical optimization algorithm was created as part of the EGOPS version v5.4, but is also still used in the v5.5, so that we kept its name for convenience.

[58] The test data for evaluating the dynamic method include simulated MetOp-A data, which are called sim-MetOp hereafter, on 15 July 2008, and real RO observations from CHAMP and COSMIC on 15 January and also 15 July 2008. Due to the limited number of CHAMP measurements on single days, we included CHAMP data also from the neighbor days (14 and 16 January resp. July), in order to have

three consecutive days for more reliable statistics. The daily background fields from the analysis, forecast, and observed data were produced for 15 January from 13 to 17 January, for 15 July from 13 to 17 July, respectively (five days centered on the day of interest as introduced in section 2.2.1). COSMIC, GRACE, and MetOp-A data were used for estimating the observation-related variables (cf. section 2.3.3), though MetOp-A data were not available for January so those observation-related variables were calculated from COSMIC and GRACE only (the difference is essentially negligible, as we confirmed by tests leaving out individual satellite data sets also in July; the results were not sensitive to leaving out a limited fraction of profiles from the large ensembles).

[59] The total number of sim-MetOp events generated for 15 July was 723. The ECMWF operational analysis fields were used for the atmospheric modeling and the NeUoG model was used as the background ionosphere model [e.g., Leitinger *et al.*, 1996; Gobiet and Kirchengast, 2004; Steiner and Kirchengast, 2005]. Two simulations were performed: 1) for perfect conditions in which the ionospheric contribution to the measurements and the observational noise were neglected, and 2) for moderate ionospheric conditions (F10.7 solar activity index in NeUoG set to 140) and the observational errors representing MetOp/GRAS-type receiving system errors (precise orbit determination (POD) errors, receiver thermal noise, local multipath, clock instabilities) following the proven settings by Steiner and Kirchengast [2005], also recently used by Schweitzer *et al.* [2011]. For these sim-MetOp data, the profiles retrieved from the first “perfect” simulation were used as the reference profiles for the results from the second “realistic” simulation.

[60] The total numbers of processed CHAMP RO events for 14 to 16 January and 14 to 16 July are 580 and 663, respectively. The total numbers of processed COSMIC RO events for 15 January and 15 July are 2992 and 2450, respectively. For profiles retrieved from these real observed RO data, their colocated ECMWF analysis profiles were used as reference profiles for the results.

[61] For both the simulated and the real RO data, both the new dynamic statistical optimization schemes, termed “Dynamic SO”, and the existing OPSv5.4 scheme, termed “OPSv5.4 SO”, were applied, in order to enable intercomparison of these two data streams. The resulting retrieved profiles were compared to their colocated reference profiles, focusing on retrieval-minus-reference differences of the statistically optimized bending angle profiles α_{SO}^k and also inspecting the subsequently retrieved refractivity and dry temperature profiles. Relative difference profiles (retrieved-minus-reference divided by reference, unit [%]) were typically produced for bending angle and refractivity, and absolute retrieved-minus-reference difference profiles for dry temperature.

[62] These differences profiles were then used to also calculate statistics for large-scale geographic regions (global and five latitude bands; see subsection 3.3), where the mean systematic difference and its associated standard deviation of the difference profiles were inspected in a comparative way for the “Dynamic SO” and “OPSv5.4 SO” results. We now first look at individual example profiles to get some basic insight how the new dynamic method works (subsection 3.2), then turn to the statistical results (subsection 3.3), and finally specifically inspect the influence of the choice of correlation matrix (subsection 3.4).

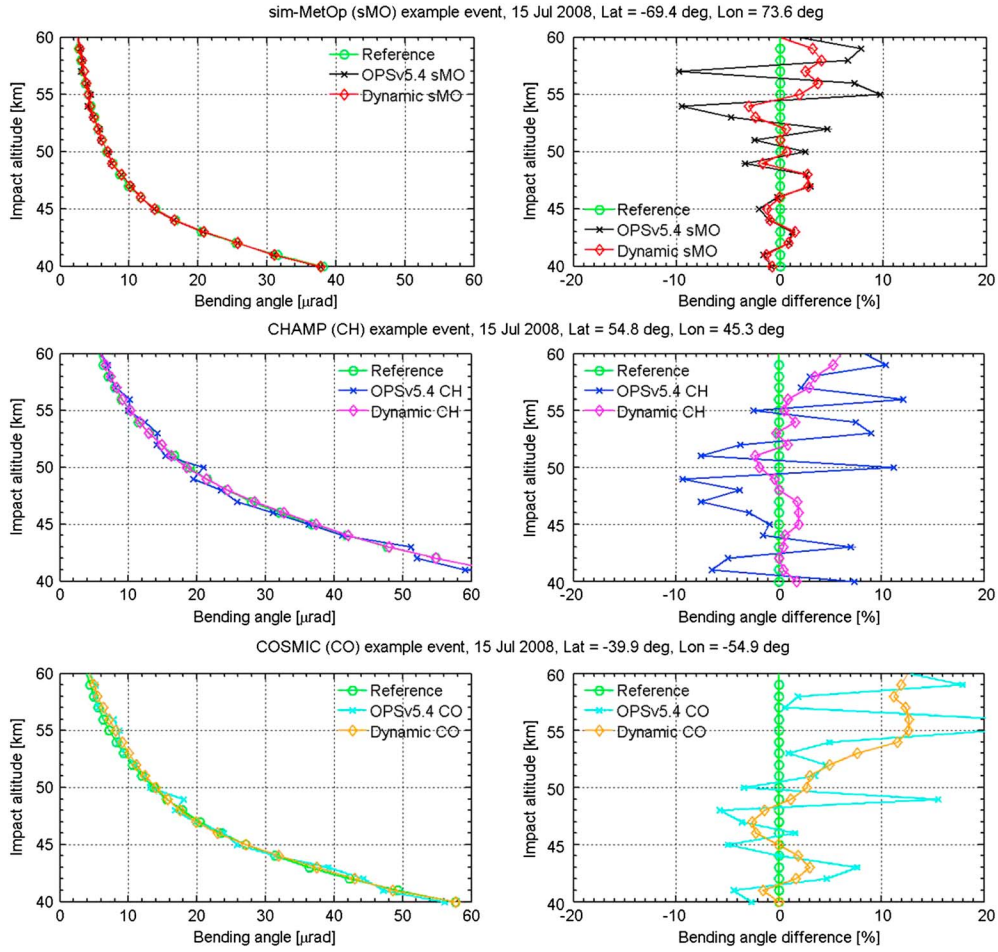


Figure 5. Statistically optimized bending angle profiles together with a reference profile (left), and their difference to the reference profile (right), of three typical example events from sim-MetOp (sMO, top), CHAMP (CH, middle), and COSMIC (CO, bottom) on 15 July 2008, obtained from the new dynamic algorithm (“Dynamic”) and the existing OPSv5.4 algorithm (“OPSv5.4”). The reference profile (“perfect” simulated profile for sim-MetOp or colocated ECMWF analysis profile for observed CHAMP and COSMIC; green) enables to gauge the quality of the respective statistically optimized profiles.

3.2. Inspecting Individual Bending Angle Profiles

[63] Figure 5 shows the statistically optimized bending angle profiles of three typical example events from sim-MetOp, CHAMP, and COSMIC, obtained from the new dynamic algorithm and the existing OPSv5.4. Absolute profiles together with their reference profile (left) as well as relative differences to the reference profile (right) are depicted. The profiles from the Dynamic SO are evidently smoother than those from the OPSv5.4 SO and they are also closer to their reference profile in these three cases. We find that there are other events, where profiles from the OPSv5.4 SO are closer to the reference profiles than from the Dynamic SO (not shown). However, profiles optimized by the Dynamic SO are generally smoother also in those cases.

[64] Figure 6 illustrates the results of some key intermediate variables of the new dynamic approach for the sim-MetOp event (the upper nine panels) and the COSMIC event (the bottom nine panels) shown in Figure 5. For each of the two events, the first row shows the estimated uncertainty of the mean analysis (left), mean observed (middle), and mean background (right) bending angle, respectively (u_a , equation

(8); u_o , equation (9); u_b , equation (6); all interpolated to the RO event location but suppressing the upper index k , like in u_b^k , for clarity here, since it does not yet occur in equations (6), (8), and (9)). The second row shows the estimated random uncertainty of the forecast (left), combined standard uncertainty of the background (middle), and relative uncertainty of the background (right) bending angle, respectively (s_{f-a}^k , section 2.2; u_b^{occ} , equation (13); $100 \cdot (u_b^{occ}/\alpha_b^k)$, equations (11) and (13)). The third row shows the estimated background (left), observed (middle), and relative uncertainty of the observed (right) bending angle, respectively (α_b^k , equation (11); α_o^k , equation (10); $100 \cdot (u_o^{occ}/\alpha_o^k)$, equations (10) and (16)).

[65] For both the sim-MetOp and COSMIC event, from the first row, we can see that u_a is smaller than u_o at altitudes above about 50 km, while below 50 km u_a is larger than u_o . The background bending angle uncertainty u_b (right), thanks to optimally combining u_a and u_o by inverse-variance weighting (equation (6)), neatly achieves the least possible uncertainty over the complete altitude range, indicating the value of this part of the new dynamic design.

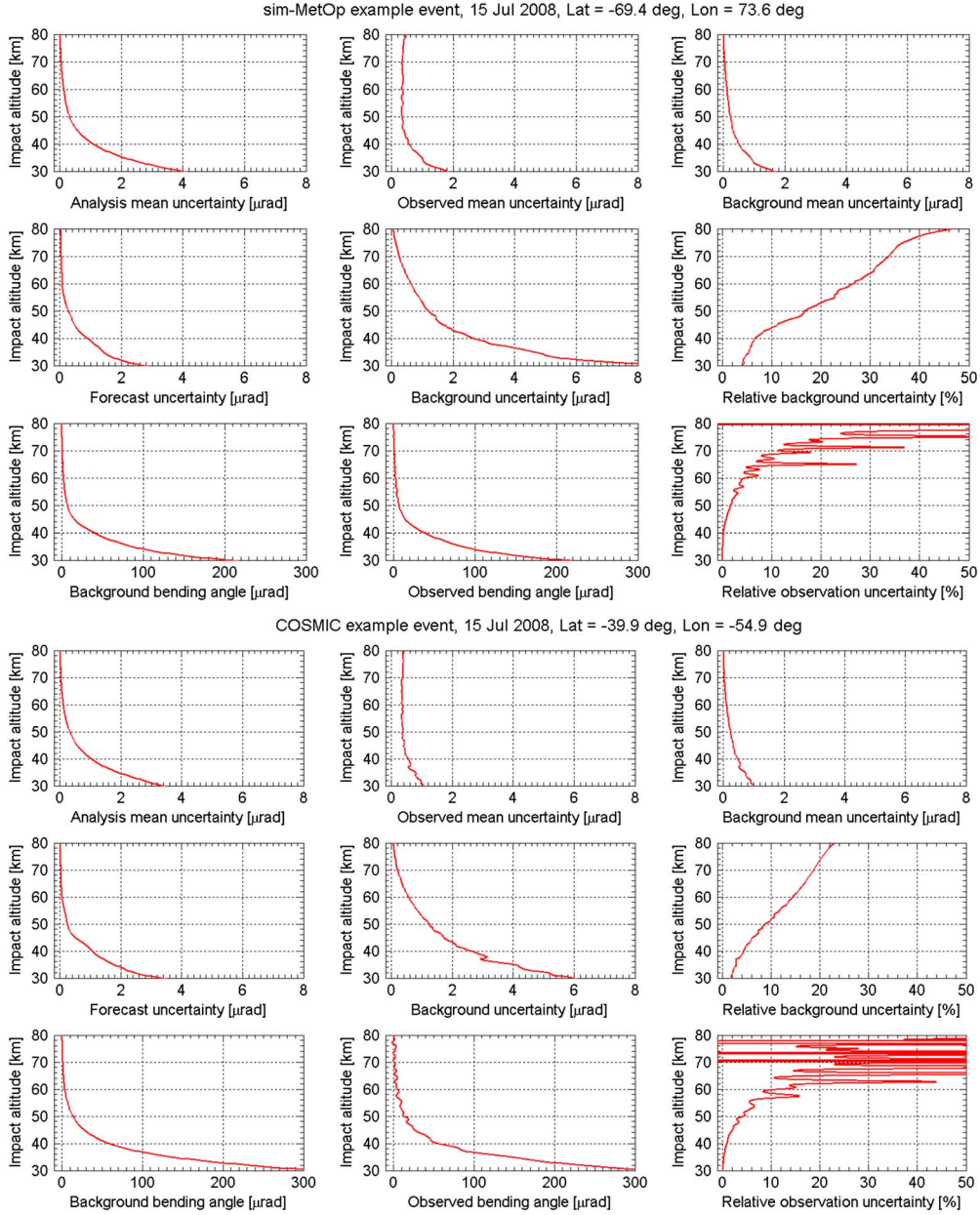


Figure 6. Illustration of intermediate variables contained in the formulation of the background error covariance matrix, for the sim-MetOp (top nine panels) and the COSMIC event (bottom nine panels) shown in Figure 5; for description see section 3.2.

[66] From the second row, again for both the sim-MetOp and COSMIC event, it can be seen that s_{f-a}^k roughly has similar magnitudes as u_a (as also indicated by comparing Figures 2 and 4, since u_a essentially corresponds to b_a), both being very small in absolute terms above about 65 km. The combined uncertainty u_b^{occ} , including now u_b (first row, right) penalized by the bias coverage factor $f_{bcvg} = 5$, is still very small in absolute terms near 80 km from which it increases to within about 5 μrad to 10 μrad near 30 km; the comparison with s_{f-a} (second row, left) and u_b (first row, right) confirms that this increase is dominated by the conservative approach that we strongly penalize the bias-type uncertainty u_b .

[67] This makes nicely explicit the relevance of how strongly the method's user decides to keep bias influences into α_{SO}^k at

bay, by choosing a certain bias coverage factor (a factor of 5 to 10 appears reasonable to us; for the purpose of this introductory study, we decided for $f_{bcvg} = 5$). Furthermore, this provides a pointer to the more general discussion of the issue of how much background information the user in general wants to weigh in for support of the high altitude initialization of α_o^k , as a separate question from the degree of (un-)certainty that is in principle available from reliable sources of background data. We defer this discussion to a follow-on study, where we additionally introduce also a more advanced observation error covariance formulation for C_o^k and larger evaluation data sets.

[68] The relative background uncertainty (second row, right) highlights that in relative terms this uncertainty strongly increases upward, exceeding 20% near 50 km for

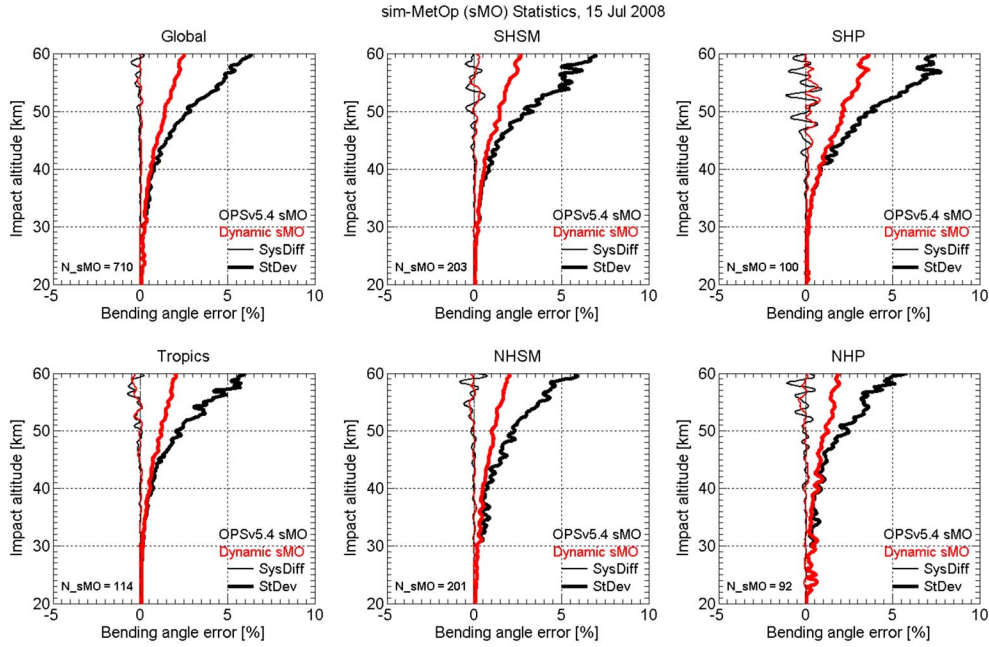


Figure 7. Systematic differences (SysDiff, light lines) and standard deviations (StDev, heavy lines) of statistically optimized bending angles, relative to “perfect” simulated bending angles used as reference, of the ensemble of sim-MetOp (sMO) events on 15 July 2008. Statistics for both the dynamic method (red) and the existing OPSv5.4 method (black) are shown for six different latitude regions: Global (90°S to 90°N), Tropics (20°S to 20°N), SHSM (southern hemisphere subtropics and midlatitudes; 20°S to 60°S), NHSM (northern hemisphere subtropics and midlatitudes; 20°N to 60°N), SHP (southern hemisphere polar latitudes; 60°S to 90°S), and NHP (northern hemisphere polar latitudes; 60°N to 90°N). The number of sim-MetOp events used to calculate the statistics in each region (N_{sMO}) is also indicated.

the sim-MetOp event and near 70 km for the COSMIC event, respectively. Such levels of difference are typical and generally driven by geographic location: in the present case the COSMIC event is located at southern midlatitudes near 40°S, where both u_b^k/α_b^k and s_{t-a}^k/α_b^k , and hence $u_b^{\text{occ}}/\alpha_b^k$ according to equation (13), are smaller than for the sim-MetOp event near 70°S (see Figures 2 and 4). Comparing these relative uncertainties to the globally static and constant relative uncertainty specifications of typically 15% or 20% in existing statistical optimization schemes (section 2.1), we see that the Dynamic SO provides the capability of significantly more realistic behavior.

[69] The third row of Figure 6, again for both the sim-MetOp and COSMIC event, confirms that α_b^k (left) and α_o^k (middle) generally go very closely together (as illustrated more directly by Figure 5 for the 40 km to 60 km impact altitude range already). The relative observation uncertainty $u_o^{\text{occ}}/\alpha_o^k$ (right) shows that, except typically for high altitudes in the mesosphere, its values are significantly smaller than the relative background uncertainty $u_b^{\text{occ}}/\alpha_b^k$ (second row, right); the “spiky” behavior of $u_o^{\text{occ}}/\alpha_o^k$ at the high altitudes is due to α_o^k with its small absolute magnitude up there (u_o^{occ} is a constant in the current formulation; see section 2.4).

[70] The detailed observation to background uncertainty ratio $u_o^{\text{occ}}/u_b^{\text{occ}}$ (not shown), and therefore also the transition altitude above which the observation uncertainties exceed the background uncertainties, depends for each RO event on the background uncertainties but more strongly on the quality of the observations (e.g., CHAMP vs. COSMIC vs.

MetOp); both aspects are well indicated by a comparative look at the relative error panels of Figure 6 and well known in principle [e.g., *Gobiet et al.*, 2007]. The more dynamic role of the background, and therefore a more adequate and realistic account for the available information, is a new feature brought in by the Dynamic SO.

3.3. Statistical Results Based on the Daily Data Sets

[71] In this section, the performance of the two statistical optimization approaches is evaluated for the full ensembles of profiles from the January and July test data sets introduced in section 3.1. The mean systematic differences in bending angle, refractivity, and temperature profiles between retrieved and reference profiles, and the associated standard deviations are analyzed. For quality control of statistical results, profiles with bending angle spikes beyond $\pm 40 \mu\text{rad}$ above 50 km, where signals are up to about $15 \mu\text{rad}$ (near 50 km) or much smaller, are rejected (as also done in preparing the observation-related variables for the daily background fields; cf. section 2.3). In addition, refractivity profiles are compared to colocated ECMWF refractivity profiles between 5 km and 35 km, and profiles differing from colocated ECMWF profiles at any altitude level by more than 10% are rejected [*Pirscher*, 2010]. Temperature profiles are also compared with their colocated ECMWF profiles within 8 km to 25 km, and profiles differing from colocated ECMWF profiles at any altitude level by more than 20 K are rejected. This is closely similar to the so-called external quality control of the OPSv5.4 processing [e.g., *Ho et al.*, 2012; *Steiner et al.*, 2013]. Based on the complete OPSv5.4 quality control

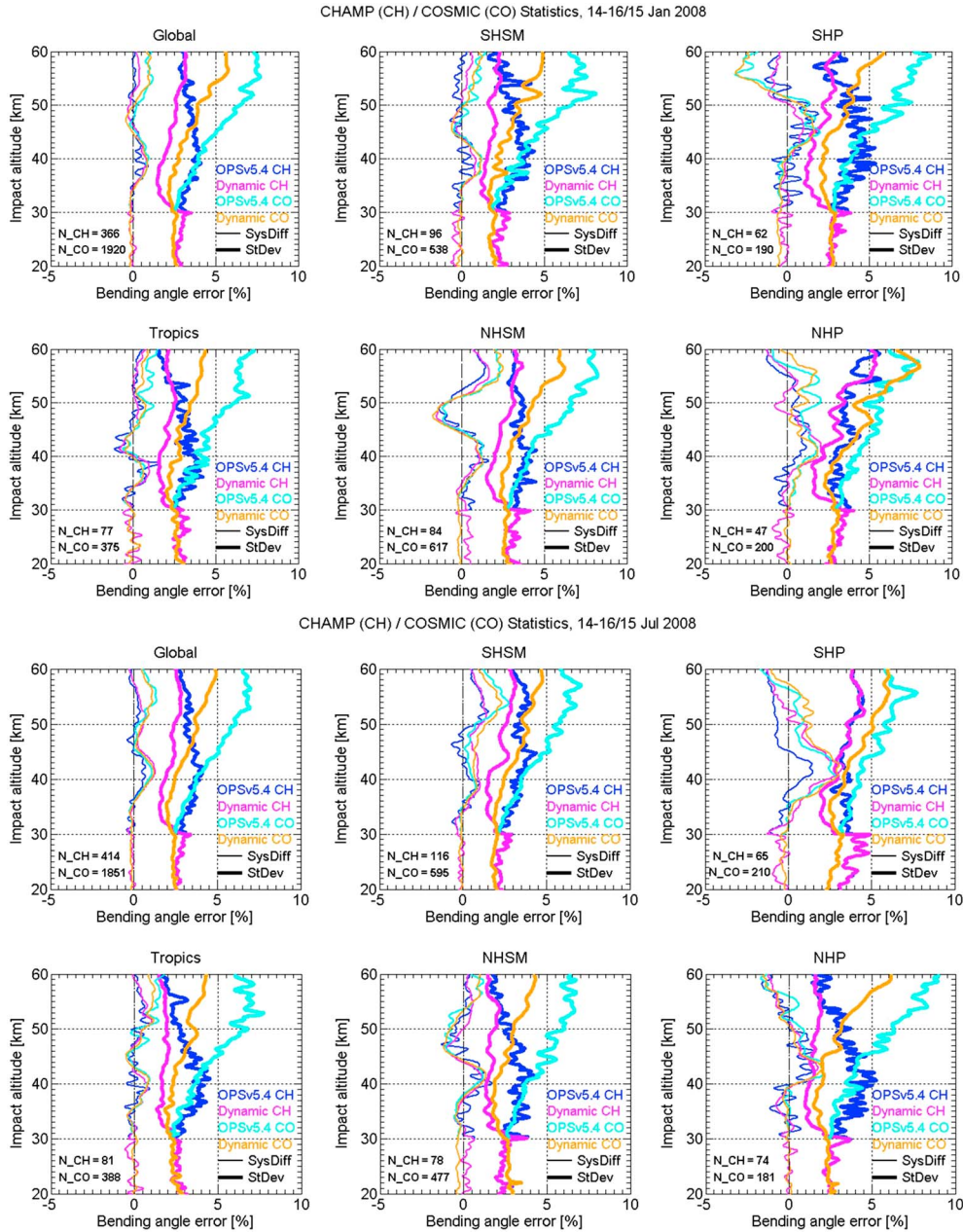


Figure 8. Systematic difference (SysDiff, light lines) and standard deviations (StDev, heavy lines) of statistically optimized bending angles, relative to colocated ECMWF analysis bending angles, of the ensembles of CHAMP (CH) and COSMIC (CO) RO events from January 2008 (top six panels) and July 2008 (bottom six panels). Statistics of both the dynamic method (magenta and orange for CHAMP resp. COSMIC) and the existing OPSv5.4 method (blue and cyan for CHAMP resp. COSMIC) are shown for the same six latitude regions as in Figure 7. The number of CHAMP and COSMIC events used to calculate the statistics in each region (N_CH resp. N_CO) is also indicated.

[Pirscher, 2010; Steiner et al., 2013] and the checks above, about 2% of the sim-MetOp profiles and more than 30% of the observed CHAMP and COSMIC profiles are identified as bad quality profiles and thus removed.

[72] Figure 7 shows the systematic difference and standard deviation profiles of all the sim-MetOp events on 15 July 2008 for six latitude regions: the whole globe (90°S to 90°N, Global), low latitudes (20°S to 20°N, Tropics), medium latitudes (20°S/N to 60°S/N, SHSM/NHSM = southern/northern

hemisphere subtropics and midlatitudes), and high latitudes (60°S/N to 90°S/N, SHP/NHP = southern/northern hemisphere high latitudes). It is clear that in all these regions the bending angle standard deviation above about 40 km retrieved from the new Dynamic SO is significantly smaller. The global mean standard deviation from the OPSv5.4 SO is larger than 6% near 60 km, which is more than twice the magnitude from the Dynamic SO being about 2.5% near 60 km. Also, and importantly, the bending angle systematic

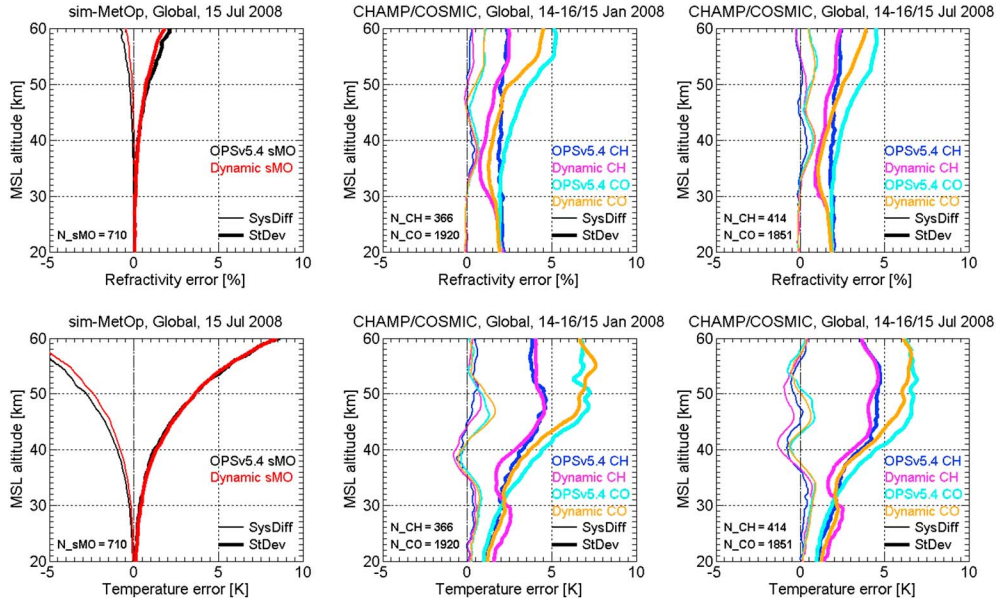


Figure 9. (Top) Refractivity and (bottom) temperature systematic differences (SysDiff, light lines) and standard deviations (StDev, heavy lines), relative to “perfect” simulated or colocated ECMWF analyses, for the global ensemble of sim-MetOp events of July 2008 (left), CHAMP and COSMIC events of January 2008 (middle), and CHAMP and COSMIC events of July 2008 (right), respectively. The figure panels are shown in the same layout as in Figures 7 and 8.

difference from the new method is smoother and otherwise essentially equal or somewhat smaller. These results for the end-to-end simulated RO events, which enable to evaluate the basic potential of the new dynamic method since the “true” reference is closely known, are very encouraging and confirm the basic capabilities of the Dynamic SO.

[73] Figure 8 shows the statistical results for the ensembles of CHAMP and COSMIC events available on the January and July test days. Due to the larger number of the COSMIC RO events and the better quality of the COSMIC receiver, COSMIC error profiles are less noisy compared to CHAMP. Intercomparing the two methods, one can see that the bending angle standard deviation from the Dynamic SO is again distinctively smaller than that from the OPSv5.4 SO in all the latitude bands both in January and July.

[74] For CHAMP data, the best improvement made by the new approach is found between about 35 km and 45 km with a reduction in the global-mean standard deviation to roughly half its value. Above about 45 km, the improvements made by the Dynamic SO decrease with height, and at 60 km both algorithms yield the same results (i.e., the background information fully dominates in both algorithms). For COSMIC data, the reduction in the standard deviation amounts to roughly one third of the values from OPSv5.4 in the impact altitude range from about 35 km up to 60 km. At the high latitudes of the winter hemisphere (NHP in January and SHP in July), where both the background and observation errors are large, the new approach shows comparatively little improvement.

[75] We note that these standard deviation results also point to the influence of the choice of bias coverage factor f_{bcvg} , i.e., the degree of intentionally inflating the bias-type uncertainty in equation (13) in order to safeguard α_{SO}^k from becoming biased: the standard deviation reduction is stronger if f_{bcvg} is comparatively smaller (for the safeguarding argument, we do

not recommend a factor below 5, though, as noted in section 3.2). In tests varying f_{bcvg} up to a factor of 10 (not shown), we found that the standard deviation reduction over the upper stratosphere becomes smaller; the systematic difference is essentially insensitive to this range of choices of f_{bcvg} , however. More discussion of potentially most adequate weightings is left to follow-on work; our current illustrative choice with $f_{bcvg}=5$ shows what we consider like the strongest reasonable standard deviation reduction.

[76] Furthermore, Figure 8 shows similar systematic differences of the RO bending angle profiles relative to the ECMWF reference profiles for both algorithms. The somewhat smoother systematic difference profiles resulting from the new algorithm, especially for CHAMP, derive from the generally smoother individual bending angle profiles from the new method (cf. Figure 5). Despite we cannot know the “truth” from these data, it is encouraging for the Dynamic SO, that despite its significant reductions in standard deviations it does not show any suspicious degradation of systematic differences; this indicates that the Dynamic SO is in principle robust against “overconstraining” with background information and that the background profiles themselves, together with their uncertainty estimates, are indeed of adequate quality.

[77] Figure 8 also reveals small “spikes” at 30 km in CHAMP’s bending angle standard deviation profiles, while such spikes are not visible in COSMIC’s. This is because at 30 km, the signal-to-noise ratio of COSMIC profiles is significantly higher than that of CHAMP (being the “worst case” in this respect given it was a pioneering early receiver), due to the higher quality of COSMIC’s onboard receivers (though detailed inspection shows that spikes also exist for some COSMIC profiles). In this study, the statistical optimization was applied exactly down to 30 km (as is the setting in OPSv5.4) so that the bending angles below 30 km are purely

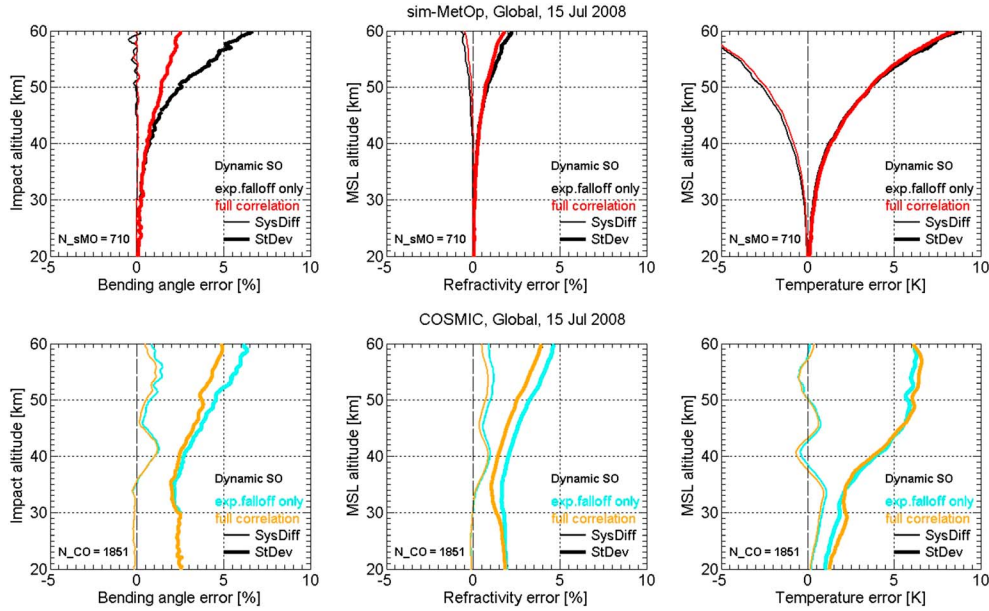


Figure 10. (Left) Bending angle, (middle) refractivity, and (right) temperature systematic differences (SysDiff, light lines) and standard deviations (StDev, heavy lines), relative to their “perfect simulated” or colocated ECMWF analysis data used as reference, of the global ensemble of (top) sim-MetOp and (bottom) COSMIC events from 15 July 2008, using either the realistic global-mean correlation matrix of the new dynamic method (“full correlation”) or simple exponential-falloff correlation as in the existing OPSv5.4 (“exp.falloff only”). The figure panels are shown in the same layout as in Figures 7 and 8.

observed bending angles. Spikes therefore occur since especially the CHAMP data quality is such that this is too high a bottom altitude for part of the profiles; or alternatively more error needs to be allowed [e.g., *Gobiet et al.*, 2007].

[78] In order to mitigate the spikes of bending angle standard deviations near 30 km, we slightly amplified the background uncertainties relative to the observation uncertainties in the altitude range from 30 km to 40 km, so that the observed bending angles would receive more weight in the resulting α_{SO}^k in this altitude range; this adjustment made a smoother transition of the CHAMP profiles above 30 km (as shown in Figure 8, otherwise the spikes would be sharper). A more consolidated future solution will include variable bottom altitudes of the statistical optimization and robust observation-to-background uncertainty ratio constraints enabling higher error from comparatively more noisy profiles in a controlled way.

[79] Figure 9 shows the global-mean errors of refractivity and temperature profiles obtained from all the three missions and the two methods. The sim-MetOp systematic differences in refractivity and their standard deviations resulting from the new method are somewhat smaller, with the largest improvement at high altitudes but consistent small improvement overall. Slight but systematic improvement is also found for the systematic differences for sim-MetOp temperature profiles; this is again encouraging for the climatological utility of the Dynamic SO. Due to the downward propagation of errors by the Abelian integral and the hydrostatic integral [e.g., *Rieder and Kirchengast*, 2001; *Gobiet and Kirchengast*, 2004; *Steiner and Kirchengast*, 2005], the absolute improvement in these retrieved variables is limited for sim-MetOp, since the OPSv5.4 SO already achieves a temperature bias of within 1 K at 40 km for these high-quality simulated data.

[80] The results for CHAMP and COSMIC thus look different and no conclusions can be made from these data on whether the systematic differences have been improved in the retrieved refractivities and temperatures, since we have no sufficiently accurate “truth” as reference. We can therefore note at this point that the climatological performance of the Dynamic SO in the retrieved variables appears at least as good as from the OPSv5.4 SO, with the capability to improve upon as indicated by the sim-MetOp results. The standard deviations are clearly reduced also in refractivity and temperature, in particular in the upper stratosphere, though the reduction is less salient than in the bending angle, again due to the downward integrations by the Abelian and hydrostatic integrals. The temperature standard deviations for CHAMP and COSMIC below 30 km are seen to be higher from Dynamic SO than from OPSv5.4 SO. Tests showed that this appears to be a side effect of the above discussed “spikes” in bending angles near 30 km, from the current simplified bottom altitude treatment, which tends to leave more standard deviation in retrieved temperatures. We note that the effect vanishes when using a more consolidated bottom altitude treatment (including improved formulation of observation error correlations, as we introduce in follow-on work), so we do not discuss it further here.

3.4. Effect of Realistic Relative to Exponential-Falloff Correlation Functions

[81] Here we investigate the differences in the RO retrievals caused by two different background error correlation matrices: 1) the empirically estimated global-mean correlation matrix \mathbf{R}_{f-a} of the new dynamic method described in sections 2.2 and 2.3, and 2) the simple analytical correlation matrix constructed by exponential-falloff correlation

functions (i.e., the exponent term in equation (15)) with a background error correlation length of 10 km as used in the existing OPSv5.4 scheme. The Dynamic SO scheme is run for this specific investigation, for case 1 just as is and for case 2 with \mathbf{R}_{f-a} replaced by the exponential-falloff correlation matrix but otherwise identical settings to case 1; so the only difference is the different correlation matrix.

[82] Figure 10 displays the comparison of the statistically optimized bending angle, refractivity, and temperature results from sim-MetOp and COSMIC for the two different cases. We see that the bending angle standard deviations, and to a smaller degree also the systematic differences, of sim-MetOp and COSMIC (left panels) are significantly reduced when using the realistic \mathbf{R}_{f-a} instead of the simple exponential-falloff formulation. For example, sim-MetOp standard deviations are reduced to roughly half their values within 50 km to 60 km, and COSMIC standard deviations to roughly 80% of their values. This indicates the value of an appropriate specification of the background error correlation functions, consistent with the error characteristics of the (ECMWF) background profiles used.

[83] Compared to the improvements in bending angles from the realistic \mathbf{R}_{f-a} , the associated improvements in refractivity (middle panels) and temperature (right panels) are smaller but still clearly visible for the refractivity; for the temperature, they are very small. A closer look at the refractivity, also compared to the respective panels in Figure 9 in particular for sim-MetOp, reveals that the systematic difference benefits less than the standard deviation, since the former is more dependent on the downward propagation of bending angle errors via the Abelian integral rather than the details of the correlations (the matrix diagonal is the same in cases 1 and 2). The reason for the very small improvements in temperature retrievals is that temperatures are again more sensitive to the downward propagation of bias-type errors rather than to details of error correlations, since there is additionally the hydrostatic integration.

[84] Overall, these effects of the correlation function formulations, realistic vs. simple exponential-falloff, clearly indicate that the use of a realistic empirically estimated background error correlation matrix as part of the new dynamic method is definitely useful.

4. Summary and Conclusions

[85] This study introduced a new dynamic approach of estimating the background bending angle and its associated error covariance matrix for obtaining statistically optimized RO bending angle profiles by an optimal estimation scheme combining this background information with the observed information. The dynamic method accounts for dependencies of background variables and their uncertainties on latitude, longitude, altitude, and day of year. It uses bending angles from multiple days of ECMWF short-range forecast and analysis fields, together with mean observed bending angles, to obtain background profiles and associated error covariance matrices with geographically and vertically varying background uncertainty estimates on a daily updated basis.

[86] We described the new dynamic method in detail, which consists of three main algorithmic steps, including: 1) construction of basic daily background fields of key analysis-, forecast-, and observation-related variables on a global

latitude-longitude-altitude grid for any day to be processed, 2) preparation of derived daily background fields with the specific statistical quantities directly needed for the statistical optimization, and 3) performing the actual dynamic statistical optimization for all RO events of any given day.

[87] We discussed the key advancements the new dynamic scheme over existing statistical optimization schemes, which include: 1) we use a 3D- and time-dependent formulation of all key statistical variables needed in the formulation of the background error covariance matrix, based on reliable ensembles of atmospheric forecast and analysis profiles as well as of observed profiles, while existing formulations use globally static relative errors and either climatologies (still most common) or forecasts (OPSv5.4) or observations (climatological profile retrievals only); 2) we use background bias estimation, allowing to actively reduce biases in the collocated background profile, while existing schemes use no such bias mitigation measure; 3) we use estimates of background bias uncertainty and random uncertainty, and penalize the former against the latter to minimize bias influence on the resulting optimized profile, while existing schemes use globally static relative background errors; 4) we use a daily updated realistic background error correlation matrix, empirically estimated from forecast-minus-analysis difference profiles, while existing schemes either ignore these correlations or use crude (exponential) falloff models not representing realistic correlation shapes.

[88] We showed furthermore that the dynamic method is flexible in a seamless manner to either include mean-analysis or mean-observed bending angle profiles and associated uncertainties or both of them together in the formulation of mean-background profile and uncertainty estimation. Based on this versatility, users of the method can readily decide which information to include according to their context and preferences. Also, the grid definition, and the space- and time-averaging domains per grid cell, can be flexibly adjusted by users.

[89] Based on all this set of advantages, we expect the new dynamic scheme to outperform existing schemes and performed first intercomparisons and an evaluation against the existing Wegener Center OPSv5.4 scheme, which is a leading existing scheme and therefore a suitable reference. We operated both algorithms, the new dynamic and the existing OPSv5.4 one, down to 30 km and used several days of simulated MetOp and observed CHAMP and COSMIC data, for January and July conditions, as test data set for this first performance evaluation.

[90] Our findings for the new method's performance compared to OPSv5.4 include: 1) the dynamic method significantly reduces random uncertainties (standard deviations) in the resulting statistically optimized profiles and also leaves less or about equal residual systematic uncertainties (biases); 2) the realistic dynamic (daily) estimate of the background error correlation matrix alone already systematically improves the quality of the optimized bending angles, compared to using simply exponential-falloff correlations; 3) the subsequently retrieved refractivity profiles and atmospheric (temperature) profiles, while seeing reduced magnitude of improvement due to the filtering through the Abelian and hydrostatic integrals, clearly benefit from the improved error characteristics of the optimized bending angles. In summary, the evidence from this first evaluation of the new method suggests that it already now outperforms

the existing OPSv5.4 method, while at the same time having considerable further development potential.

[91] Tapping on this further potential, and encouraged by the promising results of this first study, our current follow-on work focuses on employing similar dynamic error covariance estimation also for the observed bending angles and to apply the method to full months, for testing more rigorously the performance over weekly scales and in monthly means. Also, the issue of providing the most adequate level of background information in support of the high altitude initialization of the observed RO information for the various different missions with different receiver performances is a relevant aspect of the further developments. After consolidation of the dynamic algorithm, we intend to apply it as one of the essential new algorithmic components in the next Wegener Center reprocessing of the entire RO climate record, which aims at unprecedented quality of the data up into the mesosphere.

[92] **Acknowledgments.** We thank M. Bonavita and S.B. Healy (ECMWF Reading, UK) for valuable advice related to ECMWF's analysis and forecast data and associated error characteristics. Y.L. acknowledges the China Scholarship Council (CSC) for providing a scholarship for studying at RMIT University. Furthermore, we acknowledge the funding support by the Australian Space Research Program (ASRP2), the Australian Research Council (ARC) (LP0883288), and the Australian Antarctic Science (AAS4159) Program projects endorsed to a research consortium led by SPACE, RMIT at the RMIT side, and the funding support by the European Space Agency (ESA) project OPSGRAS and the Austrian National Science Fund (FWF) projects BENCHCLIM (P22293-N21) and DYNOC (T620-N29) at the WEGC side. We also thank UCAR/CDAAC for access to their RO excess phase and orbit data as well as ECMWF for access to their analysis and forecast data.

References

- Anthes, R. A. (2011), Exploring Earth's atmosphere with radio occultation: Contributions to weather, climate, and space weather, *Atmos. Meas. Tech.*, **4**, 1077–1103, doi:10.5194/amt-4-1077-2011.
- Anthes, R. A., et al. (2008), The COSMIC/FORMOSAT-3 mission: Early results, *Bull. Am. Meteorol. Soc.*, **89**, 313–333, doi:10.1175/BAMS-89-3-313.
- Ao, C. O., A. J. Mannucci, and E. R. Kursinski (2012), Improving GPS radio occultation stratospheric refractivity retrievals for climate benchmarking, *Geophys. Res. Lett.*, **39**, L12701, doi:10.1029/2012GL051720.
- Bassiri, S., and G. A. Hajj (1993), Higher-order ionospheric effects on the GPS observables and means of modeling them, *Manuscr. Geod.*, **18**, 280–289.
- Bonavita, M., L. Raynaud, and L. Isaksen (2011), Estimating background-error variances with the ECMWF Ensemble of Data Assimilations system: Some effects of ensemble size and day-to-day variability, *Q. J. R. Meteorol. Soc.*, **137**, 423–434, doi:10.1002/qj.756.
- Carter, B. A., K. Zhang, R. Norman, V. V. Kumar, and S. Kumar (2013), On the occurrence of equatorial F-region irregularities during solar minimum using radio occultation measurements, *J. Geophys. Res. Space Physics*, **118**, 892–904, doi:10.1002/jgra.50089.
- Cucurull, L., and J. C. Derber (2008), Operational implementation of COSMIC observations into NCEP's global data assimilation system, *Wea. Forecasting*, **23**, 702–711, <http://journals.ametsoc.org/doi/abs/10.1175/2008WAF2007070.1>.
- Danzer, J., B. Scherllin-Pirscher, and U. Foelsche (2013), Systematic residual ionospheric errors in radio occultation data and a potential way to minimize them, *Atmos. Meas. Tech.*, **6**, 2169–2179, doi:10.5194/amt-6-2169-2013.
- Dee, D. P., et al. (2011), The ERA-Interim reanalysis: Configuration and performance of the data assimilation system, *Q. J. R. Meteorol. Soc.*, **137**, 553–597, doi:10.1002/qj.828.
- Foelsche, U., and B. Scherllin-Pirscher (2012), Development of bending angle climatology from RO data, CDOP Visiting Scientist Report 14, Danish Meteorol. Inst., Copenhagen, Denmark.
- Foelsche, U., B. Pirscher, M. Borsche, G. Kirchengast, and J. Wickert (2009), Assessing the climate monitoring utility of radio occultation data: From CHAMP to FORMOSAT-3/COSMIC, *Terr. Atmos. Ocean. Sci.*, **20**, 155–170, doi:10.3319/TAO.2008.01.14.01(F3C).
- Foelsche, U., B. Scherllin-Pirscher, F. Ladstädter, A. K. Steiner, and G. Kirchengast (2011), Refractivity and temperature climate records from multiple radio occultation satellites consistent within 0.05%, *Atmos. Meas. Tech.*, **4**, 2007–2018, doi:10.5194/amt-4-2007-2011.
- Fritzer, J., G. Kirchengast, and M. Pock (2011), End-to-End Generic Occultation Performance Simulation and Processing System version 5.5 (EGOPS 5.5) Software User Manual, *Tech. Rep. ESA/ESTEC-1/2011*, Wegener Center and IGAM/Inst. of Physics, Univ. of Graz, Graz, Austria.
- Gleisner, H., and S. B. Healy (2013), A simplified approach for generating GNSS radio occultation refractivity climatologies, *Atmos. Meas. Tech.*, **6**, 121–129, doi:10.5194/amt-6-121-2013.
- Gobiet, A., and G. Kirchengast (2002), Sensitivity of atmospheric profiles retrieved from GNSS occultation data to ionospheric residual and high-altitude initialization errors, *Tech. Rep. ESA/ESTEC-1/2002*, Inst. for Geophys., Astrophys., and Meteorol., Univ. of Graz, Graz, Austria.
- Gobiet, A., and G. Kirchengast (2004), Advancements of Global Navigation Satellite System radio occultation retrieval in the upper stratosphere for optimal climate monitoring utility, *J. Geophys. Res.*, **109**, D24110, doi:10.1029/2004JD005117.
- Gobiet, A., G. Kirchengast, G. L. Manney, M. Borsche, C. Retscher, and G. Stiller (2007), Retrieval of temperature profiles from CHAMP for climate monitoring: Intercomparison with Envisat MIPAS and GOMOS and different analyses, *Atmos. Chem. Phys.*, **7**, 3519–3536, doi:10.5194/acp-7-3519-2007.
- Gorunov, M. E. (2002), Ionospheric correction and statistical optimization of radio occultation data, *Radio Sci.*, **37**(5), 1084, doi:10.1029/2000RS002370.
- Hajj, G. A., E. R. Kursinski, L. J. Romans, W. I. Bertiger, and S. S. Leroy (2002), A technical description of atmospheric sounding by GPS occultation, *J. Atmos. Sol. Terr. Phys.*, **64**, 451–469, doi:10.1016/S1364-6826(01)00114-6.
- Hajj, G. A., C. O. Ao, B. A. Iijima, D. Kuang, E. R. Kursinski, A. J. Mannucci, T. K. Meehan, L. J. Romans, M. de la Torre Juarez, and T. P. Yunck (2004), CHAMP and SAC-C atmospheric occultation results and intercomparisons, *J. Geophys. Res.*, **109**, D06109, doi:10.1029/2003JD003909.
- Healy, S. B. (2001), Smoothing radio occultation bending angles above 40 km, *Ann. Geophys.*, **19**, 459–468, doi:10.5194/angeo-19-459-2001.
- Healy, S. B., and J. R. Eyre (2000), Retrieving temperature, water vapour and surface pressure information from refractive-index profiles derived by radio occultation: A simulation study, *Q. J. R. Meteorol. Soc.*, **126**, 1661–1683, doi:10.1002/qj.49712656606.
- Healy, S. B., and J.-N. Thépaut (2006), Assimilation experiments with CHAMP GPS radio occultation measurement, *Q. J. R. Meteorol. Soc.*, **132**, 605–623, doi:10.1256/qj.04.182.
- Hedin, A. E. (1991), Extension of the MSIS thermosphere model into the middle and lower atmosphere, *J. Geophys. Res.*, **96**, 1159–1172, doi:10.1029/90JA02125.
- Ho, S.-P., et al. (2009), Estimating the uncertainty of using GPS radio occultation data for climate monitoring: Intercomparison of CHAMP refractivity climate records from 2002 to 2006 from different data centers, *J. Geophys. Res.*, **114**, D23107, doi:10.1029/2009JD011969.
- Ho, S.-P., et al. (2012), Reproducibility of GPS radio occultation data for climate monitoring: Profile-to-profile inter-comparison of CHAMP climate records 2002 to 2008 from six data centers, *J. Geophys. Res.*, **117**, D18111, doi:10.1029/2012JD017665.
- Hocke, K. (1997), Inversion of GPS meteorology data, *Ann. Geophys.*, **15**, 443–450, doi:10.1007/s00585-997-0443-1.
- Isaksen, L., J. Haseler, R. Buizza, and M. Leutbecher (2010), The new Ensemble of Data Assimilations, *ECMWF Newsl.*, **123**, 17–21.
- Kursinski, E. R., et al. (1996), Initial results of radio occultation of Earth's atmosphere using the global positioning system, *Science*, **271**, 1107–1110, doi:10.1126/science.271.5252.1107.
- Kursinski, E. R., G. A. Hajj, J. T. Schofield, R. P. Linfield, and K. R. Hardy (1997), Observing Earth's atmosphere with radio occultation measurements using the Global Positioning System, *J. Geophys. Res.*, **102**, 23,429–23,465, doi:10.1029/97JD01569.
- Ladreiter, H. P., and G. Kirchengast (1996), GPS/GLONASS sensing of the neutral atmosphere: Model independent correction of ionospheric influences, *Radio Sci.*, **31**, 877–891, doi:10.1029/96RS01094.
- Lauritsen, K. B., S. Syndergaard, H. Gleisner, M. E. Gorunov, F. Rubek, M. B. Sørensen, and H. Wilhelmson (2011), Processing and validation of refractivity from GRAS radio occultation data, *Atmos. Meas. Tech.*, **4**, 2065–2071, doi:10.5194/amt-4-2065-2011.
- Le Marshall, J., Y. Xiao, R. Norman, K. Zhang, A. Rea, L. Cucurull, R. Secamp, P. Steinle, K. Puri, and T. Le (2010), The beneficial impact of radio occultation observations on Australian region forecasts, *Aust. Meteorol. Oceanogr. J.*, **60**, 121–125.
- Leitinger, R., J. E. Titheridge, G. Kirchengast, and W. Rothleitner (1996), A 'simple' global empirical model for the F layer of the ionosphere (in German; English version available from the authors), *Kleinheubacher Ber.*, **39**, 697–704.
- Liu, C., et al. (2013), Characterization of residual ionospheric errors in bending angles using GNSS RO end-to-end simulations, *Adv. Space Res.*, **52**, 821–836, doi:10.1016/j.asr.2013.05.021.

- Lohmann, M. S. (2005), Application of dynamical error estimation for statistical optimization of radio occultation bending angles, *Radio Sci.*, *40*, RS3011, doi:10.1029/2004RS003117.
- Luntama, J.-P., G. Kirchengast, M. Borsche, U. Foelsche, A. K. Steiner, S. Healy, A. von Engel, E. O'Clérigh, and C. Marquardt (2008), Prospects of the EPS GRAS mission for operational atmospheric applications, *Bull. Am. Meteorol. Soc.*, *89*, 1863–1875, doi:10.1175/2008BAMS2399.1.
- Mannucci, A. J., C. O. Ao, X. Pi, and B. A. Iijima (2011), The impact of large scale ionospheric structure on radio occultation retrievals, *Atmos. Meas. Tech.*, *4*, 2837–2850, doi:10.5194/amt-4-2837-2011.
- Pirscher, B. (2010), Multi-satellite climatologies of fundamental atmospheric variables from radio occultation and their validation (PhD thesis), *Sci. Rep. 33-2010*, Wegener Center Verlag, Graz.
- Rieder, M. J., and G. Kirchengast (2001), Error analysis and characterization of atmospheric profiles retrieved from GNSS occultation data, *J. Geophys. Res.*, *106*, 31,755–31,770, doi:10.1029/2000JD000052.
- Rocken, C., et al. (1997), Analysis and validation of GPS/MET data in the neutral atmosphere, *J. Geophys. Res.*, *102*, 29,846–29,866, doi:10.1029/97JD02400.
- Rocken, C., W. Schreiner, S. Sokolovskiy, and D. Hunt (2009), Ionospheric errors in COSMIC radio occultation profile, paper presented at the 89th Annual Meeting, *Am. Meteorol. Soc.*, Phoenix, Ariz., 14 Jan.
- Rodgers, C. D. (1976), Retrieval of atmospheric temperature and composition from remote measurements of thermal radiation, *Rev. Geophys.*, *14*(4), 609–624, doi:10.1029/RG014i004p00609.
- Rodgers, C. D. (2000), *Inverse Methods for Atmospheric Sounding Theory and Practice*, World Scientific Publ., Singapore, doi:10.1142/9789812813718.
- Scherllin-Pirscher, B., A. K. Steiner, G. Kirchengast, Y.-H. Kuo, and U. Foelsche (2011a), Empirical analysis and modeling of errors of atmospheric profiles from GPS radio occultation, *Atmos. Meas. Tech.*, *4*, 1875–1890, doi:10.5194/amt-4-1875-2011.
- Scherllin-Pirscher, B., G. Kirchengast, A. K. Steiner, Y.-H. Kuo, and U. Foelsche (2011b), Quantifying uncertainty in climatological fields from GPS radio occultation: An empirical-analytical error model, *Atmos. Meas. Tech.*, *4*, 2019–2034, doi:10.5194/amt-4-2019-2011.
- Schreiner, W., C. Rocken, S. Sokolovskiy, S. Syndergaard, and D. Hunt (2007), Estimates of the precision of GPS radio occultations from the COSMIC/FORMOSAT-3 mission, *Geophys. Res. Lett.*, *34*, L04808, doi:10.1029/2006GL027557.
- Schweitzer, S., G. Kirchengast, M. Schwaerz, J. Fritzer, and M. E. Gorbunov (2011), Thermodynamic state retrieval from microwave occultation data and performance analysis based on end-to-end simulations, *J. Geophys. Res.*, *116*, D10301, doi:10.1029/2010JD014850.
- Simmons, A., S. M. Uppala, D. Dee, and S. Kobayashi (2007), ERA-Interim: New ECMWF reanalysis products from 1989 onwards, *ECMWF Newsl.*, *110*, 25–35.
- Sokolovskiy S., and D. Hunt (1996), Statistical optimization approach for GPS/MET data inversions, paper presented at the URSI GPS/MET workshop, Union Radio Sci. Int., Tuscon, Ariz.
- Steiner, A. K., and G. Kirchengast (2004), Ensemble-based analysis of errors in atmospheric profiles retrieved from GNSS occultation data, in *Occultations for Probing Atmosphere and Climate*, edited by G. Kirchengast, U. Foelsche, and A. K. Steiner, pp. 149–160, Springer, Berlin-Heidelberg.
- Steiner, A. K., and G. Kirchengast (2005), Error analysis for GNSS radio occultation data based on ensembles of profiles from end-to-end simulations, *J. Geophys. Res.*, *110*, D15307, doi:10.1029/2004JD005251.
- Steiner, A. K., G. Kirchengast, and H. P. Ladreiter (1999), Inversion, error analysis and validation of GPS/MET occultation data, *Ann. Geophys.*, *17*, 122–138, doi:10.1007/s00585-999-0122-5.
- Steiner, A. K., G. Kirchengast, U. Foelsche, L. Kornblueh, E. Manzini, and L. Bengtsson (2001), GNSS occultation sounding for climate monitoring, *Phys. Chem. Earth Part A*, *26*, 113–124, doi:10.1016/S1464-1895(01)00034-5.
- Steiner, A. K., B. C. Lackner, F. Ladstädter, B. Scherllin-Pirscher, U. Foelsche, and G. Kirchengast (2011), GPS radio occultation for climate monitoring and change detection, *Radio Sci.*, *46*, RS0D24, doi:10.1029/2010RS004614.
- Steiner, A. K., et al. (2013), Quantification of structural uncertainty in climate data records from GPS radio occultation, *Atmos. Chem. Phys.*, *13*, 1469–1484, doi:10.5194/acp-13-1469-2013.
- Syndergaard, S. (2000), On the ionosphere calibration in GPS radio occultation measurements, *Radio Sci.*, *35*, 865–883, doi:10.1029/1999RS002199.
- Untch, A., M. Miller, M. Hortal, R. Buizza, and P. Janssen (2006), Towards a global meso-scale model: The high-resolution system T799L91 and T399L62 EPS, *ECMWF Newsl.*, *108*, 6–13.
- von Engel, A., G. Nedoluha, G. Kirchengast, and S. Bühler (2003), One-dimensional variational (1-D Var) retrieval of temperature, water vapor, and a reference pressure from radio occultation measurements: A sensitivity analysis, *J. Geophys. Res.*, *108*(D11), 4337, doi:10.1029/2002JD002908.
- von Engel, A., S. B. Healy, C. Marquardt, Y. Andres, and F. Sancho (2009), Validation of operational GRAS radio occultation data, *Geophys. Res. Lett.*, *36*, L17809, doi:10.1029/2009GL039968.
- Vorob'ev, V. V., and T. G. Krasil'nikova (1994), Estimation of the accuracy of the atmospheric refractive index recovery from Doppler shift measurements at frequencies used in the NAVSTAR system, *Izvestiya, Atmos. Oceanic Phys.*, *29*, 602–609.
- Ware, R., et al. (1996), GPS Sounding of the atmosphere from Low Earth Orbit: Preliminary results, *Bull. Am. Meteorol. Soc.*, *77*, 19–40, doi:10.1175/1520-0477(1996)077<0019:GSOTAF>2.0.CO;2.
- Wickert, J., et al. (2001), Atmosphere sounding by GPS radio occultation: First results from CHAMP, *Geophys. Res. Lett.*, *28*, 3263–3266.
- Wickert, J., T. Schmidt, G. Beyerle, R. König, C. Reigber, and N. Jakowski (2004), The radio occultation experiment aboard CHAMP: Operational data analysis and validation of vertical atmospheric profiles, *J. Meteorol. Soc. Jpn.*, *82*, 381–395, doi:10.2151/jmsj.2004.381.
- Yue, X., W. S. Schreiner, J. Lei, C. Rocken, D. C. Hunt, Y.-H. Kuo, and W. Wan (2010), Global ionospheric response observed by COSMIC satellites during the January 2009 stratospheric sudden warming event, *J. Geophys. Res.*, *115*, A00G09, doi:10.1029/2010JA015466.